POLITECNICO DI TORINO

Master's Degree in Aerospace Engineering

Politecnico di Torino

Master's Degree Thesis

Design and evaluation of a propellant feed system for electric propulsion systems using aromatic hydrocarbons

Supervisor:

Prof. Lorenzo CASALINO

Co-supervisor:

Prof. Mykola IVCHENKO

Candidate:

Antonino MANGANO

December 2025

Abstract

The use of aromatic hydrocarbons as plasma thruster propellants represents a promising alternative to xenon, providing storage advantages, low ionization losses, high specific thrust, as well as low post-ionization fragmentation. However, using aromatic hydrocarbons requires significant changes at propulsion system level, in terms of storage and feeding system, and for the experimental setup, since conventional vacuum facilities for electric propulsion are designed to operate with inert gaseous propellants. The focus of the proposed project is on the design, prototyping, and evaluation of the propellant feed system based on the aromatic hydrocarbon naphthalene.

After reviewing existing feed system technologies, a design was implemented considering the physical and chemical properties of the candidate propellant and the flow theory along the system. The idea is to control the flow rate by regulating the temperature and thereby controlling the sublimation inside the tank.

A complete mechanical and thermal design of the feed system was developed, manufactured and assembled, and evaluated in a vacuum chamber setup. In particular, controlling and measuring the flow of the propellant was demonstrated, as this is the key for subsequent evaluation of the thruster performance.

Future work may include enhancements to the design and testing setup, along with a focused investigation of the pipe effect and its integration with the thruster.

Keywords

Space propulsion, Feeding system, Alternative propellants, Naphthalene, Vacuum chamber testing.

Acknowledgements

We have reached the end of a five-year journey, five intense and extraordinary years that I will carry with me forever. The end of a chapter, at last.
I want to begin these acknowledgments by expressing my sincere gratitude to all the people who have been with me.

First and foremost, a special thank you goes to my supervisors, Professor Mykola Ivchenko and Lorenzo Casalino. They have helped me tremendously, both professionally and personally, with their optimism and constant support. They never uttered a discouraging word, only encouragement and valuable advice.

To my mother. Without ever judging, she has always supported me. She always believed in me, even when I didn't.

To all my family: my sister and brother-in-law, grandparents, uncles and aunts, cousins and nephews. Their constant love and support have always reminded me that I was never alone on this journey.

To my girlfriend Martina, with whom I have the pleasure of sharing every part of my life. With unconditional love, we have supported each other through every challenge.

To my friends and colleagues, who made these past years truly special. A special mention goes to Matteo, Raffaella, Donato, Luigi, Andrea, Francesco, Simone, Saikat, Alexia, Giuditta, and Mattia. I am genuinely grateful for the wonderful bonds we have built and sharing this achievement with you means the world to me.

And finally, I wanted to thank myself. There have been many obstacles over these

years, but in the end, I am truly proud of how far I have come. While perfection may not be attainable, I am certain my resilience will never abandon me.

Onwards and upwards.

Contents

List of Figures

List of Tables

Acronyms

MFC	Mass Flow Controller
MLI	Multi Layer Insulation
PCB	Printed Circuit Board
PID	Proportional-Integral-Derivative

Chapter 1

Introduction

The purpose of the introduction is to explain the project and its objectives, while also presenting the earlier work and the methodology adopted. Based on the current development conditions, the scope of this project and the corresponding methodology are clearly defined.
The chapter further discusses the project's limitations and impacts, with particular attention to ethical and sustainability considerations.

1.1 Background & Objective

Electric propulsors typically use gaseous propellants, with xenon being the most common choice. However, alternative propellants, such as aromatic hydrocarbons, represent a promising alternative to xenon as plasma thruster propellants. They offer advantages, including improved storage capabilities, lower ionization losses, higher specific thrust, and reduced post-ionization fragmentation [4].
The challenges associated with a feed system using aromatic hydrocarbons are:

- Storage and feeding in a solid-state condition;
- Effective control of sublimation and temperature;
- Precise regulation of the flow rate;
- Handling and safety considerations, as these propellants are non-inert and dangerous for humans.

The focus of the project is the design, prototyping, and evaluation of a propellant feed

system based on naphthalene. It should work as an interface for a thruster developed by the Sant'Anna School of Advanced Studies in Pisa. The thruster is a low-power gridded ion engine that has been tested with argon and nitrogen in a flow rate range between 0.001-0.1 mg/s, but with solid propellant and heavier particle mass it seems more interesting to target higher flow rates, with a nominal operation around 0.05 mg/s. The higher flow rates could also be compatible with the Hall thruster that they are developing, which should have a nominal operating condition of 0.5 mg/s.
The objective is to develop a design capable of operating at low temperatures (up to 50-60 degrees Celsius to reach the nominal condition of 0.05 mg/s) with minimal heater power consumption, utilizing vapor pressure to produce the flow rate. The mass and dimensions must be minimized, but the main goal of this project is to develop a functional system with ample internal space to support long-term testing. Flow rate control could be achieved through temperature regulation or other mechanisms, such as needle valves or Mass Flow Controllers.
After acquiring the necessary theoretical knowledge on sublimation and flow dynamics, a system was designed and tested to characterize power consumption, temperature, pressure, and flow rate. In particular, controlling and measuring the flow of the propellant was demonstrated, as this is the key for subsequent evaluation of thruster performance.

1.2 Research questions

This project aims to answer the following questions:

- Is it possible to design an efficient feeding system for electric propulsion using aromatic hydrocarbons as propellants?
- What are the potential challenges and issues to tackle?
- What are the next challenges to face with the thruster?

The expectations include a well-functioning feeding system that can handle the challenges posed by the use of this type of propellant, or at the very least a good understanding of the problem and an attempt at different solutions.

1.3 Earlier work

Numerous research articles and PhD dissertations explore various feed systems utilizing alternative propellants such as iodine, bismuth, zinc, and adamantane. Among these, iodine and adamantane systems (as in article [5]) are particularly relevant to this project due to their solid-state storage conditions and the high vapor pressure of the propellants. Additionally, most of these studies provide methods and simulations covering the entire design process, making them valuable resources for developing a comprehensive understanding of the problem.
Furthermore, an electrothermal thruster using naphthalene serves as an interesting case study [35]. While it differs from our specific propulsor type, it offers useful insights into naphthalene storage, feeding mechanisms, and crucial handling and safety procedures.

1.4 Methodology

The method begins with a comprehensive literature review to build a solid understanding of the fundamental principles and design techniques. Based on the acquired knowledge and the characteristics of the selected propellants, a feeding system was specifically designed for our application.
The following calculations and preliminary estimations are performed to characterize the system:

- Vapor pressure of naphthalene and adamantane [4], [8], [14], [13];
- Sublimating flow rate estimation using the Hertz-Knudsen law [35];
- Choked flow rate through an orifice and comparison with the sublimation flow rate [10]. Flow control can then be achieved by modifying the temperature/orifice area or using alternative methods such as Mass Flow Controllers (MFCs);

Based on these results, it is possible to develop the preliminary ideas and identify the appropriate components. In particular, there might be some critical and delicate components, which must be verified for proper operation under a vacuum environment and under specific temperature and pressure conditions. It is also essential to determine whether all equipment can be safely placed inside the vacuum chamber,

and to identify the most suitable configuration for the test procedures.
Preliminary experimental tests are performed to characterize the system, focusing on heater power requirements, temperature monitoring, and flow behavior. These tests are conducted in a vacuum chamber and are essential for defining the parameters for the final design and testing phase. They are carried out using a simpler design and adamantane as a surrogate for naphthalene, given their similar chemical properties; therefore, fewer safety precautions are needed at the beginning.
Finally, thermal simulations (performed using Siemens NX) verifies the expected performance of the chosen design.
The final phase involves a full experimental validation of both the feeding system and thermal simulation. This includes monitoring key physical variables such as flow rate, pressure, and temperature, and identifying potential issues or improvements to be implemented.

1.5 Ethics and Sustainability

The development of a feed system for an electric propulsion system utilizing naphthalene raises both opportunities and considerations. Naphthalene, as a solid hydrocarbon, presents advantages such as ease of storage and potentially lower environmental impact compared to traditional gaseous propellants (fewer losses during storage and transport, no pressured tanks that would imply the risk of catastrophic failures or hazardous leaks in case of structural damage, etc.). However, it is also a known pollutant and classified as a possible human carcinogen [4], which requires careful handling and strict containment measures throughout the system's lifecycle. Ethically, engineers have the responsibility to ensure that any design minimizes risks to both human health and the environment, especially during the manufacturing, handling, and disposal phases. Sustainability considerations also involve assessing the full supply chain of naphthalene, including its origin, often derived from coal tar or petroleum [26], which ties into broader discussions on fossil fuel dependency. Therefore, while the system may contribute to more efficient and compact electric propulsion in space applications, it must be balanced with rigorous safety protocols and long-term environmental impact assessments.

1.6 Evaluation and News value

The primary objective of this thesis is to successfully fill the propulsor with the specified flow rate while measuring key physical parameters during testing. These measurements will help verify whether the experimental results align with our initial hypotheses and considerations. However, it is not guaranteed that the final design will work flawlessly. Therefore, the preliminary goal is to have a good understanding of how to realize the design, and to develop a feed system tailored to our chosen propellant, one that allows for accurate measurement of critical parameters. This system can later be optimized or discarded if the propellant does not meet performance expectations.
This research is significant because if the design demonstrates strong performance, it could serve as a foundation for future propulsion technologies. Even if challenges arise, the findings will be valuable in defining the limitations of the propellant. Given the potential of this technology, many companies and research institutes may find this work highly relevant and worth exploring for future applications.

1.7 Delimitations

This work is limited to the design of the feed system; therefore, future efforts should focus on the interface and integration with the pipe and the propulsion unit itself, which must be carefully evaluated and tested. Additionally, the current design does not account for the complete integration with the spacecraft and launch vehicle, which would necessitate further structural, thermal, and system-level considerations.
Future iterations of the design could aim for improved optimization in terms of mass and power consumption. This project represents an initial conceptual trial and does not yet explore the full range of possible improvements, many of which are typically identified through iterative testing and validation. Furthermore, advanced studies should be conducted to assess the behaviour of the propulsion system in the space environment, particularly under low temperatures and thermal oscillations typical of space conditions.
Safety procedures for handling the propellant in space, especially in scenarios involving human interaction, must also be clearly defined in future developments.

1.8 Outline

The upcoming chapters include the following content:

- Chapter 2: Provides background on electric propulsion, including performance metrics and propellant types.
- Chapter 3: Examines the most commonly used and alternative propellants. For alternative propellants, more detailed discussions are presented along with examples of their respective feed systems, with emphasis on naphthalene and adamantane.
- Chapter 4: Develops the feeding system design process and underlying theory and describes the flow control method. It also presents possible alternative approaches and concludes with the prototype design.
- Chapter 5: Reports preliminary tests conducted to evaluate the temperature and flow control. These tests were performed on a preliminary system and also serve to validate the flow model.
- Chapter 6: Presents thermal simulations of the designed feeding system and draws conclusions about the possible and expected behavior of the system.
- Chapter 7: Describes the final tests and presents their results, serving as an important validation of the developed design after the estimations provided by the flow model and the thermal simulations.
- Chapter 8: Summarizes conclusions and outlines directions for future work.

Chapter 2

Electric propulsion

This section provides a deeper insight into electric propulsion, its applications and performances [32]. The aim is to outline the key requirements for both the propellant and thruster design.

2.1 Electric propulsion principles

The main goal of a thruster is to achieve a specified change in velocity. In electric propulsion, electric energy is used to ionize and accelerate positive ions. There are 3 main steps to generate thrust:

1. Ionization: the production of ions, which can occur through electron emission and subsequent collisions, or via electromagnetic waves that excite free electrons and induce collisions with neutral atoms.
2. Acceleration.
3. Neutralization: the emission of electrons to maintain the overall electrical neutrality of the system.

Depending on how the acceleration takes place, there are three types of electric propulsion:

- Electrothermal: the gas is heated using electrical energy and subsequently expands through a nozzle.
- Electrostatic: ions accelerated by electrostatic forces.

- Electromagnetic: ions accelerated by electromagnetic forces.

A typical configuration for electrostatic propulsion is illustrated in Figure 2.1. It consists of a cathode and an anode at higher potential. Electrons are emitted from the cathode through thermionic emission (by heating it), and as they travel toward the anode, they collide with neutral atoms, generating ions. A discharge voltage (V_D) is applied between the anode and the cathode to maintain the electron motion. A magnetic field is used to delay the electrons from reaching the anode too quickly, increasing the probability of ionizing collisions. The cathode, the walls of the discharge chamber and the screen grid (that is the extraction grid) are held at a potential V_C, lower than the plasma potential. The accelerator grid, held at a lower potential than the screen grid, further accelerates them. Finally, a neutralizer emits electrons to maintain the overall charge neutrality of the system.

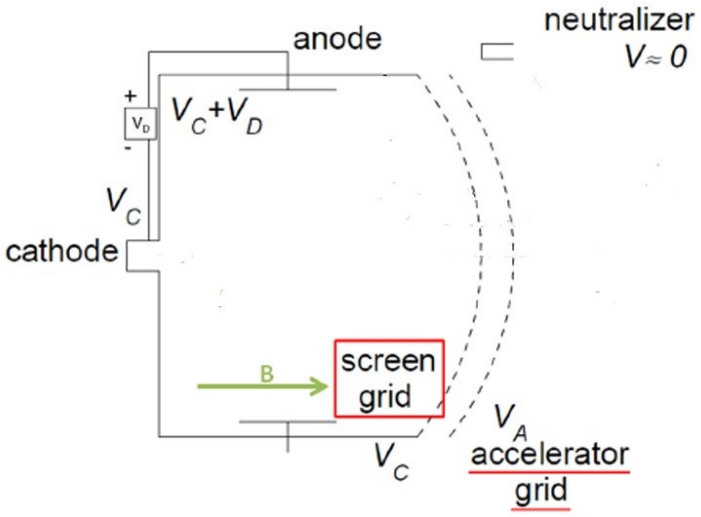

Figure 2.1: Electrostatic thruster scheme

Since the ions in the acceleration zone create a repulsive electric field for the incoming ions, there is a limit to the current density, expressed by the Child's law in the one-dimensional case:

$$j_{max} = \frac{4\epsilon_0}{9}\sqrt{\frac{2q}{m_+}}\frac{V_G^{\frac{3}{2}}}{x_a^2} \tag{2.1}$$

x_a is the coordinate measured from the screen grid and V_G is the potential difference between the screen and accelerator grid. x_a cannot be too small due to thermal load deformation and the risk of electrical sparking. Similarly, V_G cannot be too high, as this also increases the risk of sparking.

To address the limited exit current of electrostatic thrusters, Hall thrusters are widely

used. Hall thrusters belong to the family of electrostatic thrusters, although they combine both electrostatic and electromagnetic propulsion principles. In this type of thruster, acceleration occurs directly on a quasi-neutral plasma, eliminating the repulsive forces between ions. The working principle is as follows: an axial electric field and a radial magnetic field generate a drift velocity (perpendicular to both the electric and magnetic fields) and an azimuthal current along the magnetic field lines. While electrons, having a small gyro-radius, spiral along the magnetic field lines from the cathode to the anode, ions, with their larger gyro-radius, pass through the thruster exit unaffected, maintaining their motion.

2.2 Performance analysis

Assuming no gravitational or drag losses and the thrust parallel to the velocity vector, the total velocity change of a spacecraft can be determined using the Tsiolkovsky equation, also known as the rocket equation:

$$\Delta v = v_e \ln\left(\frac{m_0}{m_f}\right) \tag{2.2}$$

where v_e is the exhaust velocity relative to the spacecraft, m_0 represents the initial total mass (wet mass, including propellant), and m_f is the final total mass (dry mass, after propellant consumption).
The use of lightweight particles maximizes exhaust velocity, significantly reducing the amount of propellant required to achieve a given Δv. Table 2.1 summarizes the velocity requirements for various space maneuvers.

Mission	**Δv [km/s]**
LEO insertion	10
1-year station keeping	0.5
LEO-GEO	3.5
Earth escape	3.2
Earth-Mars	5.5

Table 2.1: Required Δv for various space missions

To evaluate the performance of a propulsion system, specific parameters are used in various spacecraft technologies. One of the most fundamental is thrust, which for electric thrusters, under the assumption of constant exhaust velocity and acceleration,

is given by:

$$F = \dot{m}_p v_e + (p_e - p_0)A_e \approx \dot{m}_p v_e \tag{2.3}$$

where $\dot{m}_p$ is the propellant mass flow rate, v_e is the exhaust velocity, p_e and p_o are the exhaust and ambient pressures, and A_e represents the cross-sectional area of the exhaust plane.

For electric thrusters, assuming singly charged propellant particles ($q = e$), Equation 2.3 simplifies to:

$$F = \sqrt{\frac{2M}{e}} I_b V_b \tag{2.4}$$

where M denotes the molecular mass of the propellant, while I_b and V_b represent the beam current and voltage, respectively [32].

This equation highlights two crucial aspects: first, unlike chemical propulsion, where energy is stored within molecular bonds, electric thrusters require an external power source to accelerate ions, increasing power demands. Second, the choice of propellant significantly influences the performance. Xenon, due to its high atomic mass (131.29 u), is commonly used, though alternative solid or non-traditional propellants may offer higher thrust potential.

Another key parameter is the specific impulse, which represents the momentum change per unit mass of expelled propellant:

$$I_{sp} = \frac{F}{\dot{m}_p g_0} = \frac{v_e}{g_0}. \tag{2.5}$$

g_o denotes the standard gravitational acceleration.

Electric propulsion systems typically achieve much higher specific impulses than chemical propulsion systems, making them significantly more efficient in propellant utilization. While chemical thrusters produce high thrust at high mass flow rates, electric propulsion achieves superior exhaust velocities with much lower propellant consumption. The specific impulse strongly depends on the propellant type; lighter propellants that can be accelerated to higher speeds enhance overall efficiency. Although xenon remains the standard choice for most electric propulsion systems, exploring alternative propellants could further enhance achievable performance.

2.2.1 Electric propulsion efficiency

The total efficiency of an electric thruster is defined as the ratio of jet power to the total supplied electrical power:

$$\eta_t = \frac{P_{\text{jet}}}{P_t}. \tag{2.6}$$

The jet power, representing the kinetic energy of the ejected particles, is given by:

$$P_{\text{jet}} = \frac{1}{2}\dot{m}_p v_e^2, \tag{2.7}$$

which can be rewritten as:

$$P_{\text{jet}} = \frac{F^2}{2\dot{m}_p}. \tag{2.8}$$

Thus, the total efficiency of an electric propulsion thruster becomes:

$$\eta_t = \frac{F^2}{2\dot{m}_p P_t}. \tag{2.9}$$

2.2.2 Advantages of electric propulsion

Thrust levels differ substantially between electric and chemical propulsion: chemical systems can produce thrust in the meganewton range, while electric propulsion operates in the micronewton to millinewton range, requiring substantial power input to enhance performance. However, electric thrusters allow for significantly higher exhaust velocities (therefore, higher Δv following Equation 2.2), despite their lower thrust-to-mass ratios.

Considering these factors, the appropriate use of electric propulsion becomes clear. Electric propulsion systems rely on power generators, which are typically heavier than those in chemical propulsion systems. However, they consume significantly less propellant. Due to their inherently low thrust and acceleration, electric thrusters require long operational durations, sometimes extending to months or even years, to achieve the desired velocity change. This characteristic makes them ideal for long-duration interplanetary missions or orbit maintenance for Low Earth Orbit (LEO) satellites, where efficiency outweighs immediate thrust needs.

For a quantitative comparison, Table 2.2, adapted from [32], presents the performance characteristics of both electric and chemical propulsion systems.

Thruster Type	I_{sp} [s]	Thrust [N]	Power [kW]	η [%]	Propellant
Chemical					
Cold Gas	50	0.1 – 100	0.05	–	N_2, Ammonia
Monopropellant	200	1 – 500	10^2	–	Hydrazine
Bipropellant	300 – 400	10^6	10^7	–	LO_2 + H_2, Kerosene
Solid	250	10^7	10^8	–	Powder (Al, Mg, Zn, S)
Electrothermal					
Resistojet	100 – 300	0.2	0.1 – 1	65 – 90	N_2, Hydrazine, Xe
Arcjet	500	0.1	1	25 – 45	Hydrazine, Ammonia
Electromagnetic					
Pulsed Plasma Thruster	850 – 1200	10^{-6}	0.002 – 0.05	7 – 13	Teflon, Mg, Mo
Electrostatic					
Gridded Ion Engine	2500 – 6000	10^{-6} – 1	0.05 – 40	40 – 80	Xe
Hall-Effect Thruster	1500 – 3000	10^{-3} – 5	0.05 – 100	35 – 70	Xe, Kr
Field-Emission Electric Propulsion	4000 – 10000	10^{-6} – 10^{-3}	0.003 – 0.09	10 – 30	In, Cs, Ga

Table 2.2: Performance characteristics of chemical and electric propulsion systems

2.3 Propellants

The first category comprises the *gaseous propellants*. These are stored in a gaseous state, which requires pressurized tanks to achieve higher storage density. Xenon represents the traditional propellant used for space propulsion due to its non-reactivity and non-toxicity, high atomic mass and good ionization properties. However, its high cost is a significant drawback. Alternatives to xenon are being investigated, for example, krypton offers lower cost, potentially higher specific impulse under optimal conditions, chemical inertness, and simple handling procedures. Nevertheless, krypton has notable disadvantages, including a much lower density and a reduced thrust-to-power ratio. Gas mixtures are being explored to develop propellants that combine the advantageous properties of different single-gas species.

Next, there is the *condensable propellants* family, where naphthalene is included. These propellants are stored in liquid or solid form, resulting in higher density and eliminating the need for pressurized tanks. However, because they are not gaseous, efficient thermal control systems equipped with sensors and heaters are required. An important property of these propellants is their vapor pressure, as a higher value leads to a greater sublimation rate from the propellant surface. A common method to model vapor pressure as a function of temperature is Antoine's equation, empirically expressed using the substance-dependent coefficients A, B, and C:

$$log_{10}(p_v) \approx A - \frac{B}{C+T} \tag{2.10}$$

This equation works well for naphthalene, as shown in the next section.

Chapter 3

Alternative propellants

In this section, alternative solid propellants are analyzed. The aim is to discuss their advantages and disadvantages and then review studies on their feeding systems to draw inspiration and identify the main design features. Therefore, only the most common and relevant systems are considered.
In the end, a complete overview and analysis of naphthalene is provided. An example of a naphthalene electrothermal thruster is also presented, which, although not identical to the thrusters considered in this project, can provide useful insights into a naphthalene feeding system.

3.1 Key properties

In Table 3.1, the key properties and characteristic values of the most relevant propellants are presented, including the most commonly used and solid alternative propellants. The following propellants are examined:

- Xenon and krypton: gaseous propellants that are the most commonly used in electric propulsion systems [32].
- Bismuth, magnesium, and zinc: solid propellants investigated and tested as alternatives to xenon. These materials can melt and sublimate when the feed system is highly heated, which is also one of the reasons why they have not yet been employed in orbit [33].
- Iodine: a solid propellant considered a promising alternative to xenon, with a moderate vapor pressure at relatively low temperatures. It has been used with

the ThrustMe NPT30-I2 iodine electric propulsion system flown onboard the NorSat-TD satellite, launched by the Norwegian Space Agency [17], [31].

- Naphthalene ($C_{10}H_8$) and adamantane ($C_{10}H_{16}$): aromatic hydrocarbons investigated and used within the scope of this project.

For electric propulsion applications, it is relevant to examine atomic/molecular mass, ionization properties, storage parameters (such as density, melting point, and vapor pressure), cost, and propellant safety.

	Xe	Kr	I	Mg	Zn	Bi	$C_{10}H_{16}$	$C_{10}H_8$
Mass [u]	131.3	83.8	126.9	24.3	65.4	209	136.2	128.2
Ionisation Properties								
First ionisation energy [eV]	12.1	14	10.5	7.6	9.4	7.3	9.23	8.14
Peak cross section [Å^2]	4.8	3.7	6.0	8.0	5.0	9.5	28	23.5
Storage and Handling								
Density STP [g/cm^3]	1.6*	0.5*	4.9	1.7	7.1	9.8	1.08	1.14
Melting Point [°C]	-112	-157	113.7	650	420	271	279	86.3
Vapor pressure at 50 °C [Pa]	-	-	316	0	0	0	104	120
Toxicity/difficulty to handle	-	-	Med.	Med.	Low	Low	Low	High
Cost [USD/kg]	1000	200	32	8.6	3.2	8.05	650	50

Table 3.1: Properties of various propellants (prices are approximate and based on the 2021-2022 market) [4], [29], [32]. *Data at 14 MPa, 50 °C.

3.2 Bismuth, magnesium, and zinc

Bismuth, magnesium, and zinc are very inexpensive propellants. Among them, bismuth has high density and atomic mass, making it especially suitable for producing high thrust.

An example of a bismuth feeding system is illustrated in Figure 3.1. A pressurized gas is used to fill the line with liquid propellant, which is further heated at the end to ensure complete evaporation before reaching the thruster anode. Heaters are also needed around the tank and the feed line to keep the bismuth liquid, while insulation reduces heat loss.

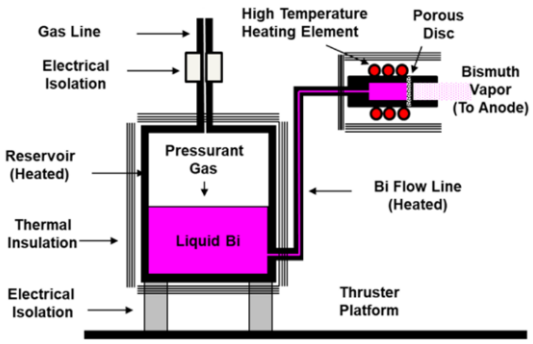

Figure 3.1: Bismuth feeding system architecture [28]

3.3 Iodine

Iodine is one of the most interesting low-cost propellants because of its high vapor pressure, which makes the evaporation process possible at lower temperatures (less power consumption). It also presents a high density and molecular mass. However, its most significant drawback lies in its reactivity and tendency to undergo chemical reactions.

Figure 3.2 shows an example of a remarkable design using this propellant, which relies on direct sublimation [17].

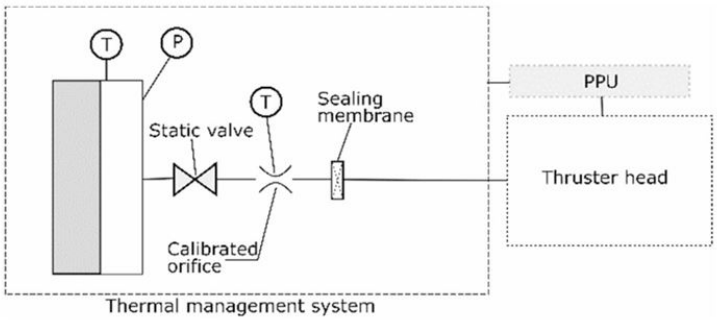

Figure 3.2: Iodine feeding system architecture

The most significant aspect is the flow control and stability, achieved using a static valve and a calibrated orifice. The static valve relies on the control of condensation and sublimation in a feedthrough insert, which becomes clogged with deposited iodine (the ”off” state) or fully unblocked (the ”on” state). Thermal regulation of the insert enables this switching behavior. The calibrated orifice enables precise control of the flow rate.

3.4 Adamantane

Adamantane offers some advantages, primarily due to its high vapor pressure and ionization properties. However, its post-fragmentation ionization is not beneficial: molecular ions break apart into multiple fragments (usually even unstable), but only one remains charged. This leads to energy losses, as part of the input energy is spent breaking molecular bonds rather than ionizing particles. For example, a high fraction (81 to 86 %) of detected naphthalene ions originate from intact molecules, while for adamantane it is only 34% [4].
The chemical structure is illustrated in Figure 3.3: there are 16 hydrogen atoms and 10 carbon atoms, represented by the vertices of the structure.

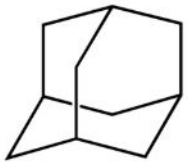

Figure 3.3: Adamantane's chemical structure [37]

A simple design with this propellant is schematized in Figure 3.4, it consists of the following components: a tank, isolating valves at both ends of the line, a purge line with a dedicated valve, and a MFC to control the flow. Heaters are incorporated to allow sublimation and prevent condensation.

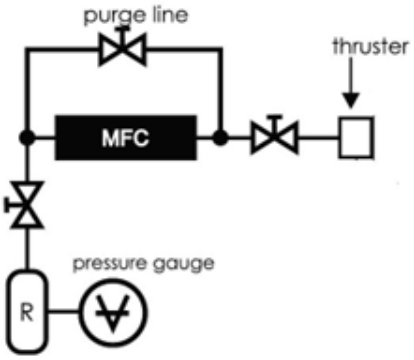

Figure 3.4: Adamantane feeding system architecture [7]

This design relies on direct sublimation of the propellant at significantly lower temperatures, taking advantage of the high vapor pressure of adamantane. The following equation, valid between 278 K and 443 K, can be used to model the vapor pressure in mmHg of adamantane [14].

$$p_v = e^{50.27 - \frac{8416}{T} - 4.211 ln(T)} \tag{3.1}$$

The curve is shown in Figure 3.5 and, as is visible comparing it with the plot in Figure 3.7, the vapor pressure is very close to that of naphthalene.

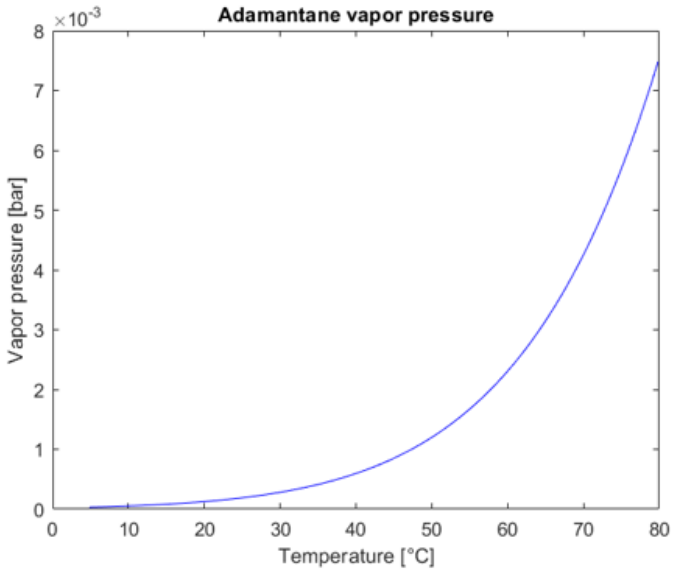

Figure 3.5: Adamantane's vapor pressure

3.5 Naphthalene

Naphthalene belongs to the family of aromatic hydrocarbons, and its chemical structure is shown in Figure 3.6. As is typical for this class of molecules, each carbon atom exhibits sp^2 hybridization, with three σ bonds and one π bond characteristic of double bonds. The stability of the molecule is enhanced by the delocalization of these π electrons across the conjugated ring system.

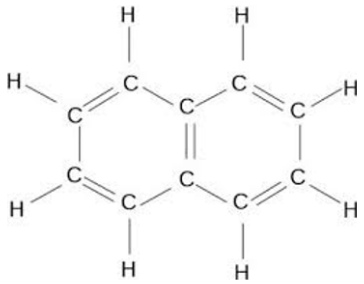

Figure 3.6: Naphthalene's chemical formula

Naphthalene offers several advantages: it evaporates at low temperatures, and its ionization properties combined with its low cost are additional benefits. However, when considering its design and integration into the spacecraft, caution is required,

as this propellant is potentially carcinogenic and generally hazardous to humans and aquatic life [4]. Therefore, it is crucial to ensure that no direct contact occurs with the propellant.

The coefficients of Antonie's law for naphthalene are shown in Table 3.2 [4], [8], [13].

Temperature [K]	A	B	C
310 to 353	8.706	2620	-52.50
353 to 452.30	4.271	1832	-61.33
399.47 to 491.79	3.971	1607	-85.92

Table 3.2: Naphthalene coefficients for Antoine's equation, pressure unity in bar except for the first row in kPa

Using Equation 2.10, it is possible to model an approximate function with MATLAB, taking the first set of coefficients for a temperature range between 37 °C and 80 °C. The function is illustrated in Figure 3.7, along with some experimental data [1] taken from the literature.

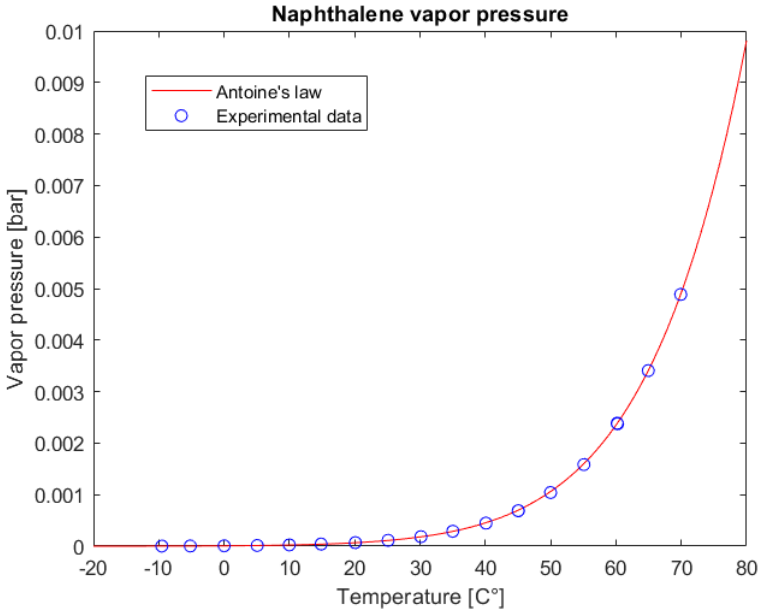

Figure 3.7: Naphthalene's vapor pressure

The Antoine model appears to work well in its temperature range and even below 37 degrees.

Figure 3.8, adapted from article [35], shows an example of a naphthalene-based electrothermal thruster. The illustration depicts a valve-controlled gas expulsion system. The reservoir, located on the left side, stores the propellant prior to release. It

is heated, and a thermocouple (T/C) is installed to monitor the temperature. O-rings are used to seal the reservoir, preventing leaks and ensuring system integrity. A spring-loaded valve plunger, actuated by a solenoid valve, regulates the gas release. Once released, the gas moves through a channel toward the nozzle throat, where resistors are placed. These resistors facilitate expansion before ejection. Another thermocouple is positioned in this region to monitor temperature variations.

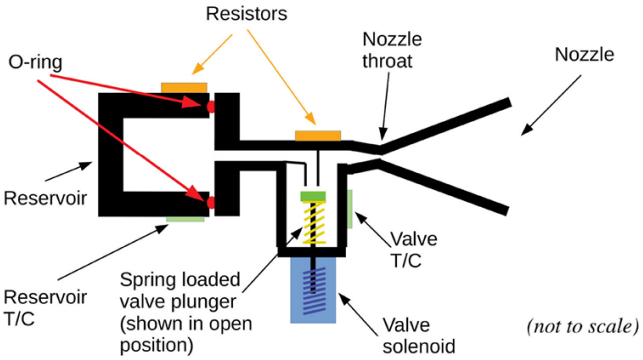

Figure 3.8: Naphthalene electrothermal thruster

Flow control takes place by regulating the temperature and the sublimation of the propellant, while the valve opens or closes the circuit. The power required to keep the thruster at 70 °C is approximately 4 W, achieving flow rates of 1-2 mg/s.
Moreover, from the previous design, valuable insights into the handling of this propellant can be gathered: once inside the vacuum chamber, the vapor produced during thruster operation is removed by a pump, ensuring no residual odor in the laboratory. To minimize exposure, the tank should be filled in a well-ventilated environment while wearing adapt personal protective equipment, such as gloves.
The design predominantly utilized aluminum, confirming the compatibility of lightweight metals with naphthalene.

Chapter 4

Feeding system

This chapter delves deeper into the feeding system using naphthalene as a propellant. The steps for selecting an appropriate design are illustrated in Figure 4.1. The process begins with defining the requirements and conducting an in-depth literature review, followed by the development of a preliminary design. The goal is to create a simple and efficient system while making use of as many available components as possible.
Before purchasing the components, preliminary tests and thermal simulations are needed to validate the feasibility of the proposed design. To fully qualify the system, final tests must be carried out.

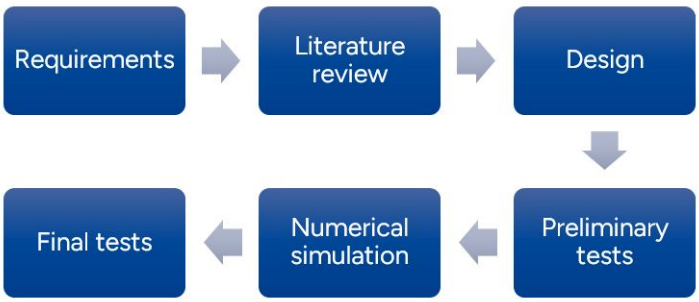

Figure 4.1: Design process

This chapter delves into the literature on flow theory and control and presents the resulting feed system prototype. The next chapters involve the preliminary tests to assess the temperature and flow control, and thermal simulations to observe how the system behaves.

4.1 Sublimation

The mass rate produced by sublimation depends on temperature T, sublimation area A, vapor pressure p_v, overlying gas pressure p_g, and molecular mass M, as expressed by the Hertz-Knudsen's law [35]:

$$\dot{m}_{subl} = \eta A(p_v(T) - p_g)\sqrt{\frac{M}{2\pi RT}} \tag{4.1}$$

An efficiency factor is included in the formula: the equation approximates an ideal case in which every molecule reaching the surface fully participates in the evaporation or condensation process. However, in reality, factors such as partial adsorption, molecular reflection, surface roughness, material defects, and energy barriers prevent a perfect interaction, making it necessary to introduce an efficiency factor to correct for these deviations.
The following assumptions and parameter values are used in this project:

- $\eta \approx 1$. This assumption should be revisited if the test results do not align with the theoretical predictions.
- p_v from Figure 3.7. As evident from the graph and discussed in the corresponding section, Antoine's law provides a reliable model for determining naphthalene vapor pressure. It is clear that the vapor pressure remains significant even at low temperatures. This represents a considerable advantage in terms of tank mass and the heating power required for space missions.
- Universal gas constant: $R = 8.314\ J/(mol \cdot K)$
- $M = 0.128$ kg/mol for naphthalene.

4.2 Orifice

Inside the tank, there is an orifice (Figure 4.2) that should be analyzed, as it determines the flow conditions.
The flow, under stagnation conditions inside the reservoir, passes through the orifice, which is choked because the upstream pressure is expected to be much higher than the downstream pressure, since an electric thruster operates at low pressure and in space

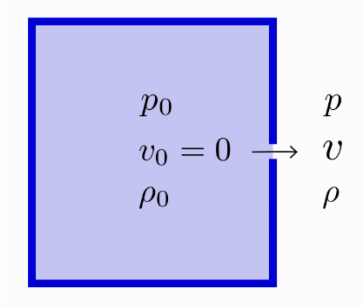

Figure 4.2: Flow rate from a reservoir through an orifice

vacuum. The orifice flow can be described using the following expression [12]:

$$\dot{m} = C_d A_{or} \sqrt{\left[2 p_0 \rho_0 \left(\frac{\gamma}{\gamma - 1}\right)\left(1 - r^{\frac{\gamma-1}{\gamma}}\right) r^{2/\gamma}\right]} \tag{4.2}$$

$r = p/p_o$ is the pressure ratio across the orifice, A_{or} is the throat area, and C_d is the discharge coefficient of the orifice. This term accounts for the non-ideality of the flow, including deviations from isentropic behavior and associated losses, since the equation is obtained for an isentropic flow (in this case, p_o and T_o are also equal to the total pressure and temperature).
Using the perfect gas equation for the density, the expression becomes:

$$\dot{m} = C_d A_{or} p_0 \sqrt{\left[2 \frac{M}{R T_0} \left(\frac{\gamma}{\gamma - 1}\right)\left(1 - r^{\frac{\gamma-1}{\gamma}}\right) r^{2/\gamma}\right]} \tag{4.3}$$

For a choked orifice, the Mach number (Ma) at the exit is equal to 1. Under this condition, the pressure inside the reservoir is related to the pressure at the orifice exit by the following equation, which is the relation between total and static pressure:

$$p_0 = p\left(1 + \frac{\gamma - 1}{2} M a^2\right)^{\frac{\gamma}{\gamma-1}} = p\left(1 + \frac{\gamma - 1}{2}\right)^{\frac{\gamma}{\gamma-1}} \tag{4.4}$$

Therefore, for the pressure ratio:

$$r = \frac{p}{p_0} = \left(\frac{2}{\gamma + 1}\right)^{\frac{\gamma}{\gamma-1}} \tag{4.5}$$

The actual tank contains the solid propellant; above its surface, the conditions correspond to the stagnation conditions. Therefore, T_o and p_o correspond to the temperature and the overlying gas pressure inside the tank T and p_g.

The final expression for the flow rate is given by [10]:

$$\dot{m} = C_d A_{or} p_g \sqrt{\frac{\gamma M}{RT}\left(\frac{2}{\gamma+1}\right)^{\frac{\gamma+1}{\gamma-1}}} \tag{4.6}$$

Being a complex molecule, for Naphthalene $\gamma \approx 1.3$.

Particular attention should be paid to the first factor in the formula, which is the discharge coefficient. As suggested in article [34], $C_d \approx 0.6$ is a reasonable and conservative approximation. Moreover, this assumption can be confirmed by looking at Figure 4.3, taken from article [38], where the commonly used curve of the coefficient with the Reynolds number is shown for a sharp-edged orifice. Although this plot excludes factors such as clearance and chamfer, it is adequate for the purpose of this analysis.

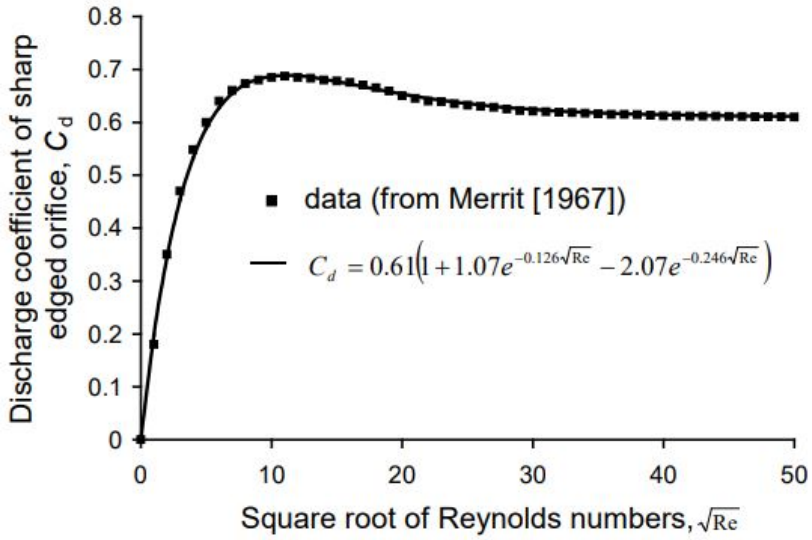

Figure 4.3: Discharge coefficient variation with Reynolds number for a sharp-edged orifice

The Reynolds number can be expressed in terms of the flow rate, the orifice diameter D, and the dynamic viscosity μ of the propellant as follows:

$$Re = \frac{4\dot{m}}{\pi D \mu} \tag{4.7}$$

For a gas, the viscosity order is maximum $10 - 100$ μPa/s in the temperature range relevant to this project [16]. The nominal flow rate ranges between 0.05 mg/s and 0.5 mg/s, with the orifice diameter on the order of millimeters. This implies that $\sqrt{\mathrm{Re}} > 20$ at minimum, corresponding to the plateau region of the graph and to $C_d \approx 0.6$, as

assumed. However, at low flow rates (low Reynolds numbers), this assumption is no longer valid and the discharge coefficient tends to zero.

4.3 Flow rate

In order to understand the pressure evolution inside the tank, it is important to consider the balance between sublimation and mass outflow through the orifice. For small orifices, the sublimation process is generally much faster than the discharge rate. Consequently, the tank pressure approaches the propellant vapor pressure. Over time, the system reaches a steady state in which the rate of sublimation exactly balances the mass leaving through the orifice. This situation can be analyzed by equating the sublimation mass flow rate (Equation 4.1, assuming unit efficiency) with the choked mass flow rate through the orifice (Equation 4.6), and simplifying the terms that appear in both expressions:

$$A(p_v - p_g)\sqrt{\frac{1}{2\pi}} = C_d A_{or} p_g \sqrt{\gamma \left(\frac{2}{\gamma+1}\right)^{\frac{\gamma+1}{\gamma-1}}} \tag{4.8}$$

This equation can be rearranged as:

$$A(p_v - p_g) = A_{or} p_g C_d \sqrt{2\pi} \sqrt{\gamma \left(\frac{2}{\gamma+1}\right)^{\frac{\gamma+1}{\gamma-1}}} \tag{4.9}$$

All the end terms can be grouped into a single coefficient:

$$k = C_d \sqrt{2\pi} \sqrt{\gamma \left(\frac{2}{\gamma+1}\right)^{\frac{\gamma+1}{\gamma-1}}} \approx 1 \tag{4.10}$$

In this way, the relation simplifies to:

$$A(p_v - p_g) = A_{or} p_g \tag{4.11}$$

It is then straightforward to express the pressure ratio as a function of the area ratio:

$$\frac{p_g}{p_v} = \frac{1}{\frac{A_{or}}{A} + 1} \tag{4.12}$$

This result shows that, for small orifices, the saturated pressure inside the tank is very close to the vapor pressure because the sublimating area is much larger than the orifice area.
Then, considering that the upstream pressure at the orifice is approximately equal to the vapor pressure, the dependence of the mass flow rate on the propellant temperature can be plotted for different orifice radii (Figures 4.4a and 4.4b). The plots correspond to the two orifice radii considered in this project: 0.3 mm and 0.4 mm. As shown, if the radius is too small, it becomes impossible to achieve the required mass flow rate at lower temperatures. However, a smaller orifice diameter enables better control of the flow rate and reduces the risk of leakage and propellant losses, particularly during the thruster cool-down phase and when the system is inactive in the vacuum of space.

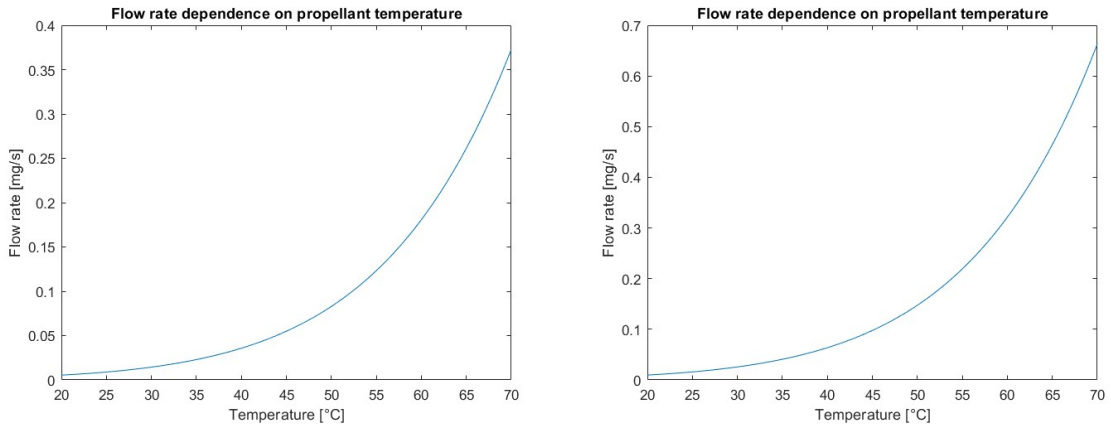

(a) Orifice radius of 0.3 mm (b) Orifice radius of 0.4 mm

Figure 4.4: Flow rate dependence on propellant temperature

4.4 Flow control

As shown in Figure 4.4, controlling the flow by regulating the temperature, known as a thermal throttle, is a promising approach. This method represents the first strategy adopted in this project. The concept for the real system involves a heated tank, where the mass flow rate can be controlled by monitoring and adjusting the temperature. When the heating is turned off, the tank cools down, causing the flow to decrease or stop.
The potential challenges to be tackled are:

1. Thermal inertia of the system. The response of the feed system must be fast

enough, giving the required flow to the thruster in an acceptable time, without requiring a large power boost too.

2. Thermal couplings and temperature distribution. The temperature should be distributed throughout the main components during thruster operation.

3. Clogging. To stop the flow without using valves, solid naphthalene should clog the orifice at low temperatures; otherwise, some losses will be present in vacuum.

Flow control can also be achieved using a needle valve or a MFC. They allow for the decoupling of the systems, which is preferable as thermal throttles are slow, have high inertia, and tend to be less accurate. However, due to the complexity and operational challenges associated with these devices, the design of the feeding system was initially based on a simpler and cheaper solution. The two most common types of MFCs for gasses, thermal-based and pressure-based, are presented in the following subsections, with the operational principles and associated challenges.

4.4.1 Thermal-based MFCs

Thermal-based MFCs measure and regulate gas flow by exploiting the relationship between mass flow rate and heat transfer. However, these devices present several limitations, including calibration accuracy, reliance on gas correction factors, and sensitivity to pressure, orientation, and temperature variations.
Figure 4.5 shows the working principle of a typical thermal-based MFC [27].

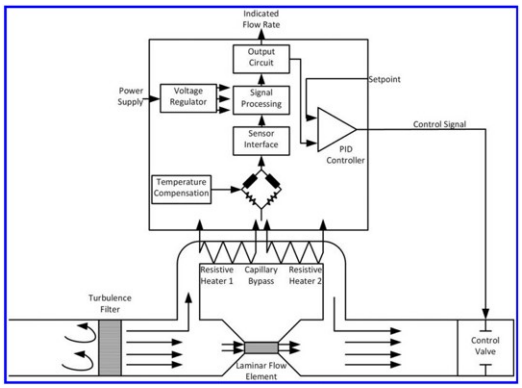

Figure 4.5: Operating scheme of a thermal-based MFC

At the inlet, a turbulence filter is used to suppress turbulent fluctuations that could affect the measurement accuracy. When the process gases flow into the MFC, a laminar flow element, illustrated in the figure as a narrowing of the flow path, causes a small

fraction of the gas to be redirected through a capillary bypass line. This portion of the flow passes through a thermal sensor before being reintroduced into the main stream. In the capillary bypass tube the flow remains laminar (otherwise, in the presence of turbulence, transient fluctuations would occur) and a known heat power P is provided to the heater coils, where temperature sensors are also placed. One way to calculate the mass flow rate is based on the temperature increase between the upstream and downstream sensors:

$$\dot{m} = \frac{P}{c_p(T)(T_i - T_o)} \tag{4.13}$$

where $c_p(T)$ is the specific heat at constant pressure, and T_i and T_o are the inlet and outlet temperatures of the heated section, respectively.

The measured flow is compared to a reference set point using a Proportional-Integral-Derivative (PID) controller. Based on the error signal, the controller adjusts the position of the control valve to regulate the flow rate accordingly.

If a thermal-based MFC is used, calibration is necessary under operational conditions, as the device relies on the heat properties of the gas, which change with operational conditions. In addition, pressure losses of the process fluid associated with the thermal tube capillary bypass are present.

4.4.2 Pressure-based MFCs

Pressure-based MFCs are used to minimize the associated sources of uncertainty. One measurement method is known as the critical (or sonic) flow method. This method relies on regulating and monitoring the upstream pressure of a calibrated orifice, in order to establish choked flow conditions, where the mass flow rate becomes independent of downstream pressure. Referring to the notation in Figure 4.6, the mass flow rate becomes directly proportional to the inlet pressure P_1, provided that P_1 is at least twice the outlet pressure P_2. Under this condition, the control valve adjusts P_1 (by a PID controller) to modulate the flow with precision as it exits the orifice into the environment. The mass flow rate can be determined according to Equation 4.6.

However, although this device is expected to be less affected by certain sources of error compared to the previous one, it introduces new uncertainties, particularly due to the integrated manometer. Moreover, the issue of pressure drop remains significant. The two most suitable MFCs are summarized in Table 4.1, where it can be observed that the pressure drop associated with the pressure-based controller is still relatively high.

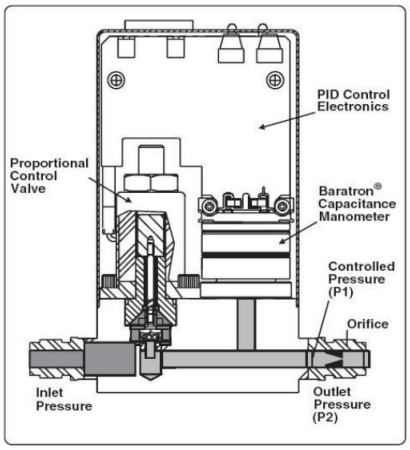

Figure 4.6: Operating scheme of a pressure-based MFC [27]

It depends on the flow rate, and the pressure drop reported in the table corresponds to the operating conditions required for this project.

Company	Controller series	Type	Pressure drop	Operating temperature
Omega	FMA-LP2600A	Pressure-based	<5.5 mbar	-10 to 50 °C
Bronkhorst	LOW-ΔP-FLOW	Thermal-based	<1 mbar	-10 to 50/70 °C

Table 4.1: Most suitable MFCs [6], [22]

As shown, thermal-based MFCs can offer advantages in terms of lower pressure drop. Another important factor to consider is the operating temperature, as the feeding system may reach temperatures exceeding 50°C.

4.5 Feeding system design

In this section, the final design of the system is presented. It should be noted that this is a preliminary version, which could be optimized in the future by reducing the overall dimensions, or integrating a more efficient heating system. For the purposes of this project, the key objective is to ensure that the system operates reliably with low power consumption. The design has been guided by the following considerations:

- A large space inside the tank is needed to test the system for a long time.
- The heat system should be distributed for heating separately the different components, resulting in less total power required.
- Several components were procured from the market. Since some of these can be expensive and have long delivery times, the choice was made to use simple and readily available parts whenever possible.

- Two different orifice diameters are considered and tested: 0.6 mm and 0.8 mm. Testing both configurations provides insight into how the orifice area affects the flow rate in practice, and helps determine the optimal option while also considering propellant losses.

Further thermal simulations are useful to evaluate the current design. Ultimately, these prototypes were experimentally tested to validate the simulation results and to assess the overall operability of the system.
The final prototype was designed using Siemens NX. It presents the following components:

- Cylindrical tank made of AL6082-T6 (Figure 4.7a). It includes four holes with a diameter of 3.3 mm (providing sufficient clearance for M3 screws) and a groove for the O-ring, designed according to ISO 3601 standards [2]. The wall thickness is minimized to reduce the energy required to heat the interior. The internal volume dedicated to the propellant is approximately 130 cm^3, which, considering the density of naphthalene from Table 3.1, allows for storing about 150 g of propellant. This quantity is sufficient to operate for about 83 hours in the worst-case scenario of a 0.5 mg/s flow rate.
  The flange area for the screws and the O-ring was minimized to ensure secure fastening between the lid and the tank, accounting only for the space required by the O-ring groove and screw heads.

- A small PCB as lid, as shown in Figure 4.7b. The material of this component is a glass fiber/epoxy composite, which is one of the reasons a PCB was chosen: it has low thermal conductivity and enables thermal decoupling from the tank. In this configuration, a large heater warms the tank, which has high thermal conductivity, ensuring a uniform temperature distribution along its surface. The lid, on the other hand, remains partially unheated. The orifice is locally heated by four small heaters (surface mounted resistors) placed on the PCB.

- An O-ring to seal the tank when closed with the lid. It has an internal diameter of 60.05 mm and a cord thickness of 1.78 mm [25].

- Stainless steel M3 screws and nuts to securely fasten the components together.

- Stainless Steel Swagelok Tube Fitting Female Connector, 1/4 in. Tube OD x 1/4 in. Female NPT [18]. This adapter connects the feed system to the thruster, and

is directly glued onto the lid.

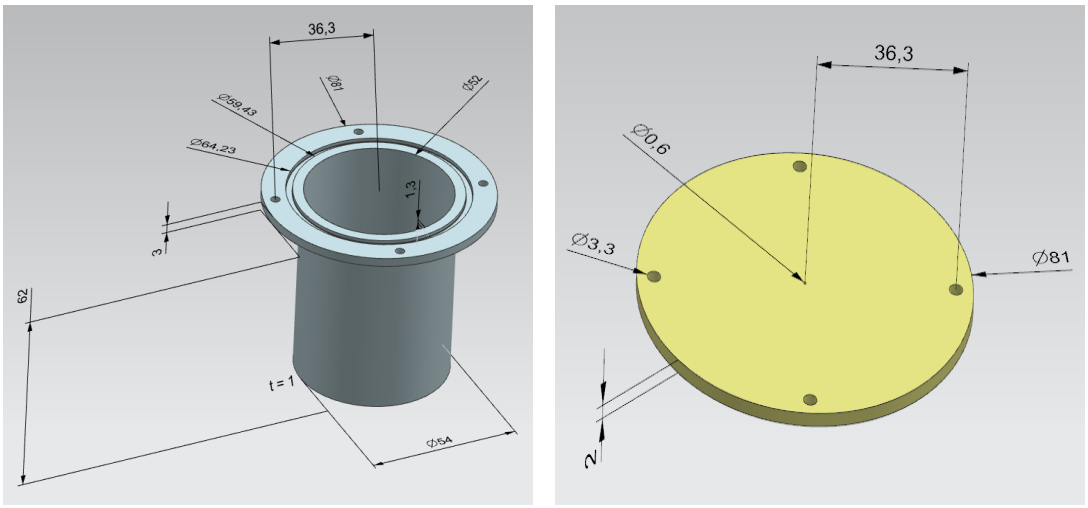

(a) Tank (b) Lid (PCB)

Figure 4.7: Tank and Lid (all dimensions in mm)

The assembly is reported in Figure 4.8.

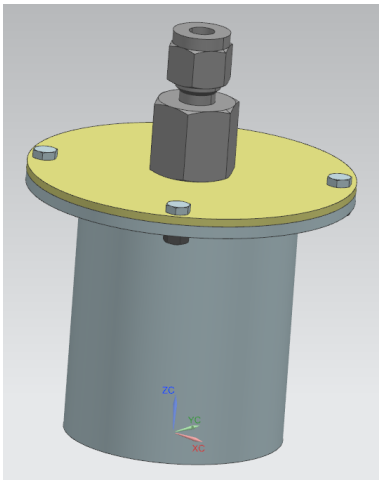

Figure 4.8: Feed system prototype

For the purposes of this project, the pipe and the interaction with the thruster are not considered. However, since the pipe is partially thermally decoupled from the other components (due to the low conductivity of the lid), the thruster affects the system only in the immediate vicinity of its end and any influence from the thruster is expected to be mainly confined to the pipe heater. This heater is necessary to account for potential thermal interactions with the thruster within the thermal control system and to prevent vapor condensation.

Chapter 5

Preliminary tests

Several experimental tests were conducted to observe the behavior of both the components and the system, and to assess whether the system can perform as expected. A preliminary basic configuration was used, since the purpose was to validate and calibrate the temperature and flow control before purchasing the components.
The preliminary experiments carried out in the vacuum chamber include:

1. *Tank heating*. A heater attached to the lateral surface of the tank warms the component, and a thermistor is used to monitor how the temperature changes with varying heater power. This is a simple and effective way to evaluate the feasibility of using the electric power to control the temperature. The tests were performed with and without the MLI, in order to observe its impact on thermal inertia and required power.

2. *Tank heating with propellant*. The tests aimed to determine how much power is required to sublimate the propellant. The temperature would be lower than for keeping the empty tank at a constant temperature (as some heat goes into gasifying the propellant).
   In addition and most importantly, with this experiment it is observable how quickly the propellant leaves the tank at different temperatures, by weighing the tank before and after the test and measuring the time. The weight can be measured using a sample holder to put inside the tank if too difficult to deal with its total mass (a precise scale would be required).

Another key test is *assessing the possible clogging of the orifice*; however, this is carried out during the tests with the final design, which includes precise thermal

control along the orifice. The hypothesis is that if the end plate with the orifice remains cooler than the saturated vapor temperature, condensation could occur there. This may cause either a negative or a positive effect. The negative is that the diameter of the orifice can be reduced or even completely clogged during normal operations. This makes the temperature control of the flow less reliable (since it is not certain whether the orifice is actually open). The positive effect is the tank "sealing" when not in use. If the orifice is cooled down before the tank, it may clog, preventing propellant loss even without an open/close valve.

5.1 Experimental setup

The preliminary system tested (Figure 5.1) consists of a long cylindrical tank, connected to a central ring, an O-ring, and a seal, with an orifice on one side having a diameter of 0.6 mm. A heater tape, illustrated in Figure 5.1 on the right (Models PI102831-00 and PI102833-00 by Backer Calesco [3]), is powered by an appropriate power supply and attached to the tank.

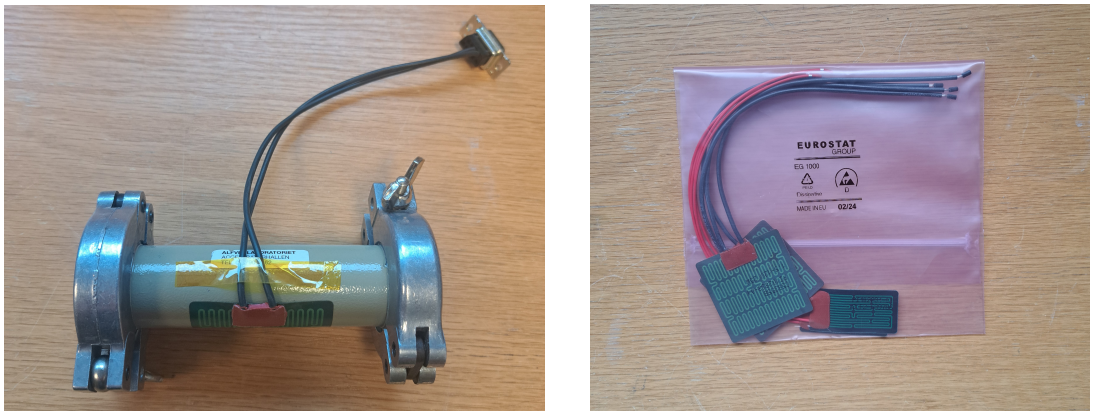

(a) Preliminary system (b) Heaters

Figure 5.1: Preliminary system and heaters

The system is placed in a small vacuum chamber without and with MLI wrapped around[1], as shown in Figure 5.2. The chamber pressure sensor is a Pfeiffer HPT 100 [24], connected to a 24 V power supply. The pressure could be measured by connecting it to a laptop via USB and using terminal software like PuTTY for serial communication.

[1]In this way, by using the contact between the tank and the MLI, it was possible to directly suspend the tank inside the chamber, thereby avoiding conductive losses between the component and the chamber floor. When MLI was not used, the system was suspended inside the chamber with a thin metal wire

(a) Vacuum chamber

(b) Assembly with MLI

Figure 5.2: Vacuum chamber and preliminary system with MLI

The temperature is measured by an NTC Thermistor (NTCALUG54A M5 by Vishay [36]). The extremity of the instrument is connected to the component with a Kapton tape (Figure 5.3).

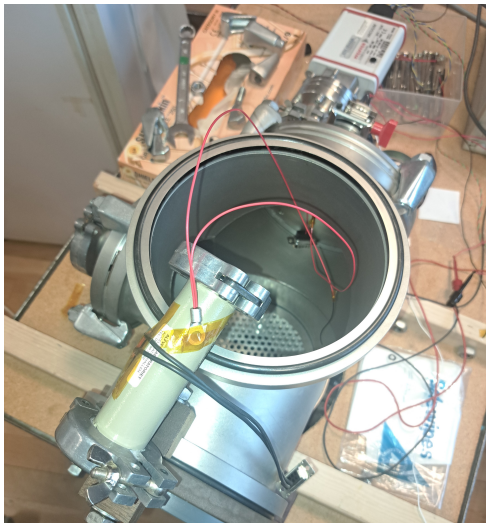

Figure 5.3: Preliminary tests: thermistor and connection with the tank

The measured thermistor resistance changes with the temperature, which can be derived using the Beta equation:

$$T = \frac{1}{\frac{1}{T_0} + \frac{1}{\beta} ln(\frac{R}{R_0})} \tag{5.1}$$

Where $T_0 = 25\ °C = 298.15$ K, $R_0 = 10\ k\Omega$, and the Beta constant of the instrument is equal to 3435 K.
To assess the validity of Beta expression, the instrument was calibrated using a thermal chamber and the temperature was set to see the corresponding resistance. The fit curve is illustrated in Figure 5.4, along with the curve obtained from the theoretical formula.

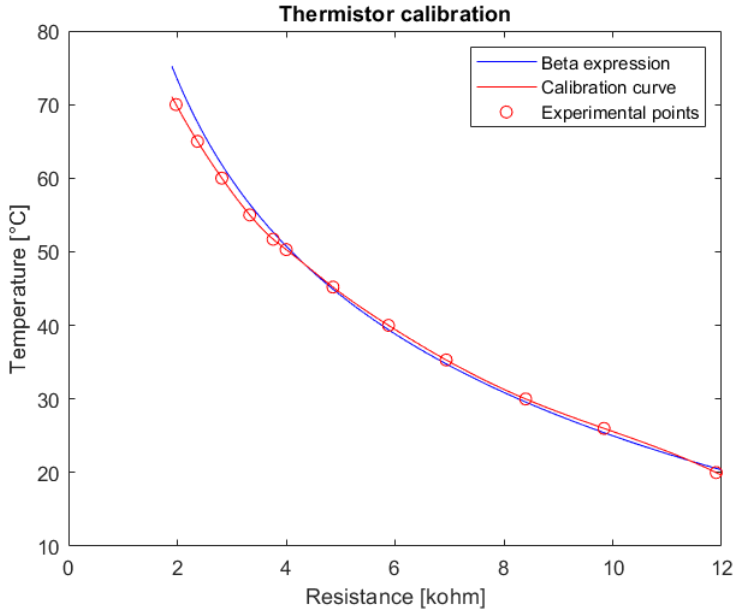

Figure 5.4: Preliminary tests: thermistor calibration and theoretical curves

The plot shows that the beta expression provides a good approximation of the temperature up to 50 °C. However, at higher temperatures, it is more accurate to rely on our calibration.

5.2 Tank tests

The system, with the electrical connections for the heater and the thermistor, was placed inside the chamber. Two different tests were carried out: one with MLI and one without.
The chamber has two pumps: the rough and the power pump, the second one used for getting high vacuum conditions. Both pumps were used for the tests, and the measured pressure during the experiment was equal to 0.005 mbar.
The ambient temperature was about 21.9 degrees Celsius.
Figure 5.5 shows the results (Appendix A.1 contains all the measurement data),

including two different plots: one on a linear scale and the other on a logarithmic x-axis. As expected, the trend shows higher power levels when not using MLI, starting from the same initial temperature. During the test, the current could only be adjusted in increments of 0.1 A, which was the minimum step size allowed by the generator.

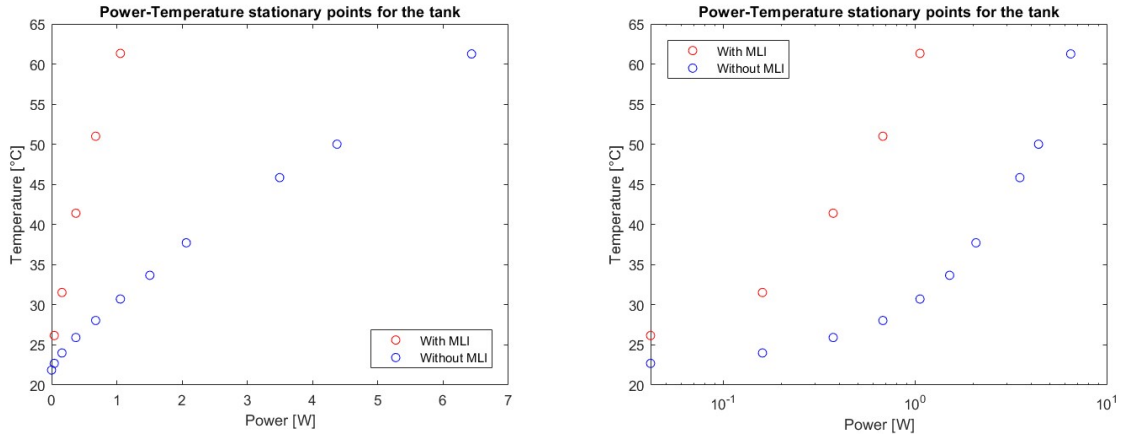

(a) Normal scale

(b) Log scale for the power

Figure 5.5: Preliminary tank tests: power-temperature stationary points

For many points, the maximum power allowed by the power supply (11 W) was used to accelerate the process. With MLI, this phase lasted approximately 10–15 minutes to reach the highest temperature point. After reaching each point, the power was reduced to allow the system to approach steady-state conditions.

However, reaching steady-state conditions still required a long time, even five hours with MLI. The delay is more noticeable when the insulator is used, which facilitates heating with minimal power input but significantly increases thermal inertia. Fortunately, the temperature reaches an almost steady state within one to two hours, with an overall variation of only a few degrees.

These tests demonstrated the effects of MLI and how temperature varies in response to changes in heating power, especially highlighting the role of thermal inertia. The thermal response of the system is very slow, suggesting that the final design should consider using a power level higher than that required for steady-state operation, in order to reach the target temperature more quickly.

In addiction, the measurements are associated with certain sources of error. Determining the steady-state points was particularly challenging, as the temperature varied very slowly toward the end of each measurement. Moreover, the thermistor was not fully attached to the tank and had a slight clearance. As a result, the observed temperatures are slightly different from the real ones.

5.3 Propellant tests

The same tests as before, with MLI, were conducted with the propellant inside the tank, under approximately the same pressure and external conditions. Adamantane was placed in a small glass container (Figure 5.6).

Figure 5.6: Adamantane used for preliminary tests

An additional thermistor was positioned near the orifice for these experiments. The results are presented in Figure 5.7 (Appendix A.2 contains all the measurement data), and in Figure 5.8 there is a comparison with the previous tests.

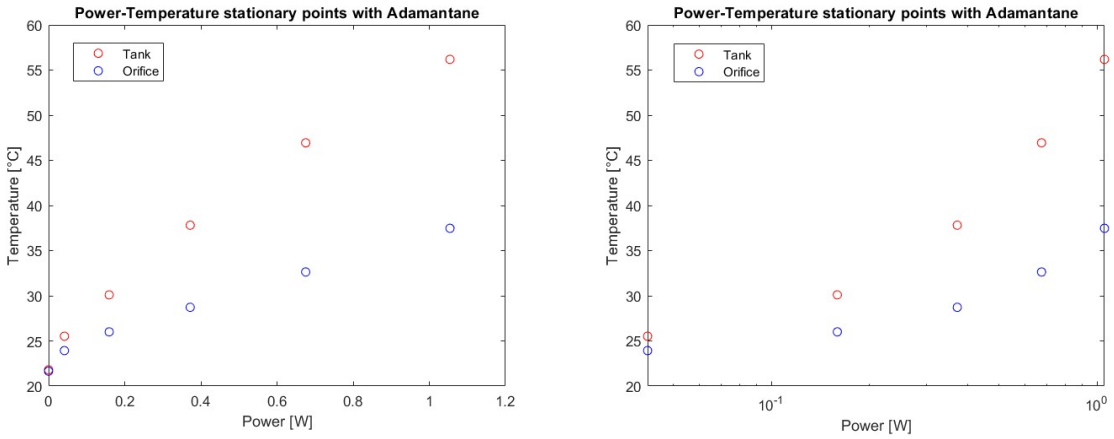

(a) Normal scale

(b) Log scale for the power

Figure 5.7: Preliminary propellant tests: power-temperature stationary points

As expected, the temperature is lower when the propellant is inside the tank. This is

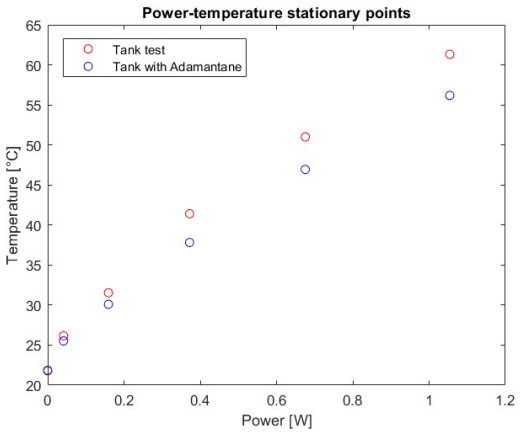

Figure 5.8: Preliminary tests: comparison between tank-only and propellant tests

due to the propellant sublimation enthalpy.
The average mass flow rate was measured by weighing the glass container before and after the tests and recording the elapsed time:

$$\dot{m} = \frac{\Delta m}{\Delta t} \tag{5.2}$$

As shown in Figure 5.9, even with this preliminary setup, a flow rate of 0.05 mg/s was achieved. The required time remained long, most of all when using MLI.

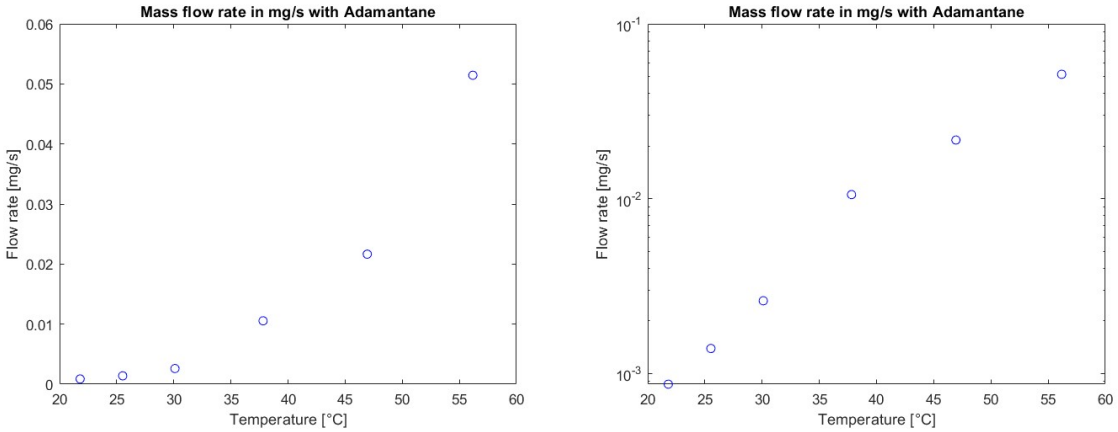

(a) Normal scale (b) Log scale for the flow rate

Figure 5.9: Preliminary propellant tests: flow rate trend with temperature

In the end, it is important to verify whether the results are consistent with the flow theory described previously. Taking into account the highest measured point, with a flow rate of 0.0514 mg/s and a corresponding tank temperature of 56.2 °C, the results do not match the expected flow rate: from Figure 4.4 it is visible that the expected flow rate at this temperature should be approximately 0.135 mg/s. This discrepancy could

be due to several factors, such as incorrect theoretical assumptions or issues within the experimental setup.

One plausible explanation arises from the temperature distribution within the system. The second thermistor, located on the orifice plug, consistently shows a lower temperature than the tank itself (Figure 5.7). The significant temperature difference, on the order of 20 °C, suggests poor thermal contact between the cylindrical wall of the tank and the end plug. It is possible that the bottom end plug is significantly colder than the walls. As a result, the propellant near or in contact with the bottom end plug could be at a lower temperature than the tank walls. This phenomenon could explain the reduced flow rate observed in the measurements.

In addiction, the presence of such cold spots inside the tank, especially around the top end plug with the orifice, could lead to local condensation of the propellant. The vapor pressure would drop toward the saturated vapor pressure corresponding to the temperature of the coldest spot. Interestingly, if this occurred, the measured flow rate would be overestimated, as the propellant condensing inside the tank (but outside the glass container) would be missing from the container. However, no condensation was observed during the tests.

Moreover, the power going into the sublimation can be estimated considering the obtained flow rate:

$$P_{subl} = \frac{\Delta H}{M}\dot{m} \tag{5.3}$$

where ΔH is the sublimation enthalpy of adamantane (approximately 55 kJ/mol [19]), and M is the molecular mass of the propellant (136.24 g/mol). Table 5.1 shows the results for every point.

Flow rate [mg/s]	**Sublimation power [W]**
0.000868	0.000350
0.00140	0.000561
0.00260	0.00110
0.0105	0.00430
0.0216	0.00870
0.0514	0.0208

Table 5.1: Preliminary tests: power going into the sublimation for every experimental point

Taking into account Figure 5.8, the estimated values appear too low to account for the temperature difference observed between the two tests, suggesting that the results could be significantly affected by uncertainties. However, the tests demonstrated both

the achievable flow rate magnitudes (at least 0.05 mg/s at temperatures below 60 °C, which is the minimum requirement) and their limits, while also providing valuable insight into the power required for propellant sublimation. They also highlighted how temperature is distributed within the components under different applied heat powers and suggested how to proceed with final tests to reduce uncertainties: allowing more time to reach steady-state conditions and using different thermistors that can be more easily attached to the components.

Chapter 6

Thermal simulation

A set of thermal simulations was performed using the NX software, with the Space Systems Thermal solver. Two cases were simulated:

- *Case 1*: the system shown in Figure 4.8 was simulated, without the final pipe. The reason is that the PCB with an orifice diameter of 0.8 mm used for the final test, which was the first unit procured, has four heaters (4.4×1.9 mm, 0.5 mm in height, positioned approximately 4 mm from the orifice), which would likely overlap with the pipe; therefore, it is not possible to glue the PCB to the pipe. However, the pipe could be added in future tests. Its contribution is expected to be minimal because of its partial decoupling from the system. The main effect would be an increase in power consumption, as a heater would be wrapped around the pipe to warm the component and account for the thruster interface.
- *Case 2*: case 1 with MLI, as using insulators would reduce power consumption. The thickness of the insulator is assumed to be 5 mm, as measured from the insulators used in the preliminary tests.

These simulations are significant for anticipating the expected behavior of the system. For each case, the steady-state temperature distribution and the transient response are presented using representative and reasonable heat load configurations. To account for the sublimation power, each steady-state simulation was iterated multiple times, as shown in the following sections.
In addition, all steady-state temperature values for the propellant, corresponding to varying heat loads on the tank and as observed during preliminary tests, are plotted.
In the transient plots, both the warm-up and the cool-down phases are reported.

6.1 Materials properties and thermal couplings

For thermal simulation, the thermal conductivities, specific heat capacities, densities, and emissivities of the materials are required. In Table 6.1, these parameters are reported.

For almost all properties, it is straightforward to find them[1]. An exception is represented by MLI, which requires a more detailed review of the literature [15]. Since no article reports the radiative properties of naphthalene, the emissivity in this project is approximated using the values available for pyrene [21], due to its analogous chemical structure. For the PCB, looking to the literature [9], the emissivity of this component could be assumed to be 0.95.

Material	k [W/m/K]	c_p [J/kg/K]	ρ [g/cm^3]	ϵ
AL6082-T6	180	900	2.7	0.31
PCB	0.3	900	1.85	0.95
NBR (O-ring)	0.25	1350	1.2	0.85
Stainless steel	15	477	7.85	0.85
Naphthalene	0.12	1311	1.14	0.9
MLI	0.07	1783.3	0.38	0.02

Table 6.1: Materials thermal properties

The emissivity properties are for wavelengths around 8 μm, since the objects temperatures are between 20 and 100 degrees Celsius (IR emissions). The absorptivity is considered equal to the emissivity (no transmitting materials).

Another important aspect is the thermal couplings between different surfaces when they touch each other. When perfect contact between surfaces is defined, NX automatically sets the thermal couplings during simulation by assuming equal interface temperatures on both sides. This assumption is considered reasonable in the presence of sufficiently strong mechanical contact, and it was adopted in the simulations.

6.2 Mesh and solver specifications

The mesh used is a 3D mesh, with TET4 elements (Figure 6.1). NX automatically sizes the elements for each object.

Each simulation is initially carried out under steady-state conditions, where the solver handles a time-independent heat transfer problem, meaning that the simulation time

[1]The aluminum emissivity used refers to naturally oxidized aluminum

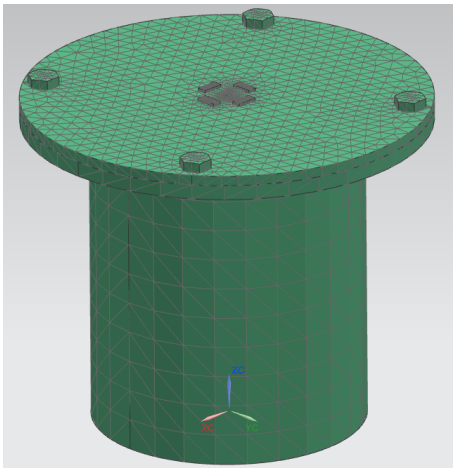

Figure 6.1: 3D used mesh for the thermal simulation

and time step are not relevant, as there is no time dependence. Subsequently, transient analyses are performed to evaluate the warm-up and cool-down phases under specific heat load scenarios.
For the first case, the default time step is set to 72 seconds, and the simulations cover a time span of 20 hours to capture the full thermal transient. In the second simulation set (with MLI) a 30-hours transient thermal response was simulated. The transient simulation is divided into two phases: the first half represents the warm-up phase, during which heat loads are applied; in the second half, the cool-down phase, the heat loads are set to zero.

6.3 Assumptions and limitations

These simplified approximations are considered for our simulation:

- No threads, nuts, and O-ring in the model to simplify the mesh.
- For the heater around the tank, a heat load (W) is set uniformly on the entire lateral surface of the component. For each heater on the orifice, a volumetric distributed heat load (W/mm^3) is imposed.
- The view factors to the environment are approximated to 1 for exposed surfaces.
- Internal radiation is considered between the propellant and the bottom part of the PCB, between the tank and the MLI, and between the MLI and the exposed faces on the lid. The view factors are calculated directly using NX.
- Naphthalene was modeled as a solid block, although in practice it is a powder.

The initial temperature (for the transient) was set at 20 degrees, as well as the environmental temperature. The ambient pressure is 0.001 mbar.
Unfortunately, the chamber walls could not be included in the model, which, combined with the assumption of the view factors to the environment, introduces a certain degree of inaccuracy. In reality, the chamber reflects radiation and emits it according to its own emissivity.
In the model, the radiative emission from a surface (W/m^2) to the environment is represented as follows, depending on the surface emissivity and the temperatures of both the surface and the environment:

$$P = \epsilon\sigma(T^4 - T_{env}^4) \tag{6.1}$$

However, in practice, the effective temperature of the system changes because of the limited emissivity of the chamber walls, the reflections, and the view factors. Despite these limitations, the simulation provides valuable insight into the temperature corresponding to a given heat input and, more importantly, highlights the temperature distribution and the thermal decoupling between components.

6.4 Heat load configurations

Table 6.2 summarizes all the simulated heat loads for each case. The loads are identical for both the transient and steady-state simulations.

Simulation number	Load on the tank [W]	Orifice heaters [W/mm^3]
1	4	0.005
2	3	0.005
3	2	0.005
4	1	0.005

Table 6.2: Heat load configuration for the simulations

Considering the ideal heater dimensions, the volumetric power of the orifice corresponds to 0.0209 W. Only for the initial simulation, two additional simulations were performed, one with the orifice heaters power doubled and one with the tank half full, and the transient behavior was recorded to assess their effect.

6.5 Case 1

This case illustrates the thermal behavior without the use of MLI. For the transient simulations, Table 6.3 shows the corresponding physical points for each node reported.

Node	Physical point
3315	Side surface of the tank
4581	Naphthalene top surface
2644	Orifice
2710	Point on the PCB far from the orifice and tank

Table 6.3: Thermal simulation case 1: nodes reported in the transient plots

With the half-filled tank configuration, only minor changes in node numbering occur: node 2644 (orifice) becomes 2643, and node 4581 (naphthalene) is updated to 4501.

6.5.1 First simulation

The resulting steady-state temperature distribution and the transient response are shown in Figures 6.2 and 6.3.

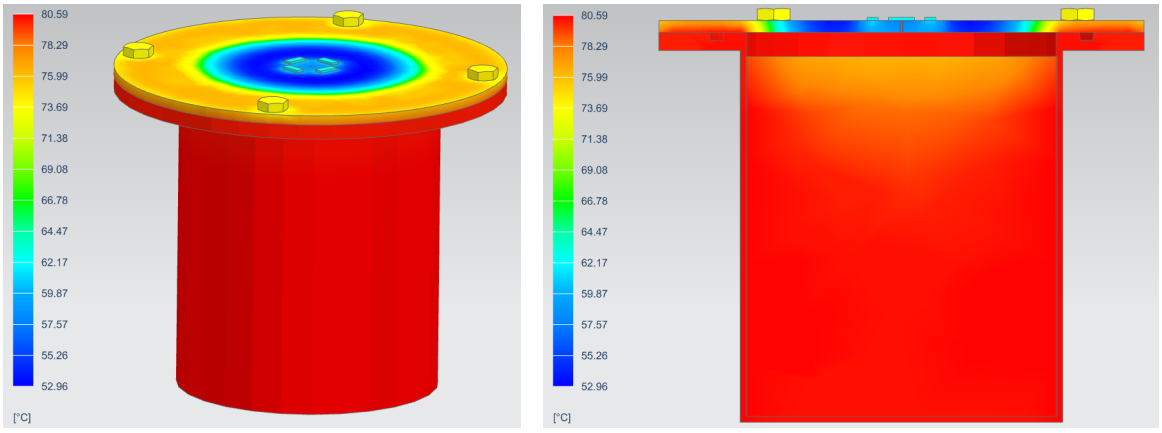

(a) Entire assembly (b) Section

Figure 6.2: Thermal simulation case 1, first simulation: steady-state temperatures

The steady-state temperature inside the propellant is about 80 degrees, but the time required to reach thermal equilibrium exceeds four hours at every reported point. In the transient plot, the cooling phase is also visible and requires a time comparable (even more) to that of the warming phase.
Only for this case, the heat fluxes are reported in Figure 6.4, where the radiative flux

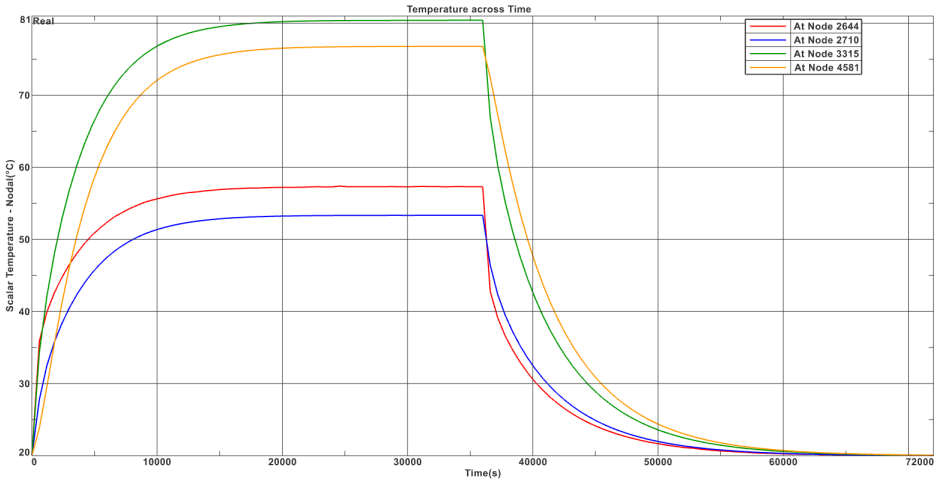

Figure 6.3: Thermal simulation case 1, first simulation: transient response

looks consistent with the temperatures along the system and the material emissivities. The heat balance is verified by looking at the simulation log file: the deviations are very low. With every stead-state simulation, the heat balance was verified.

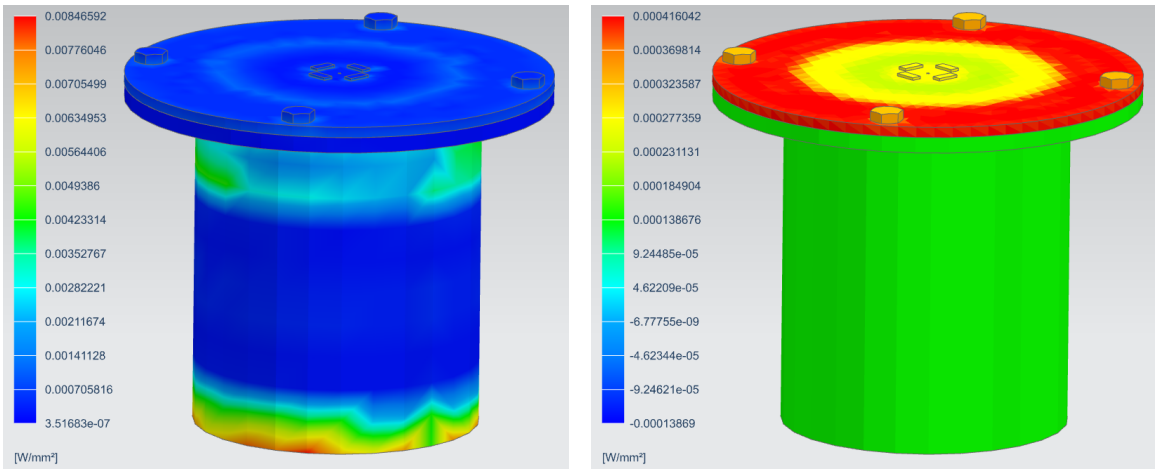

(a) Conductive flux (b) Radiative flux

Figure 6.4: Thermal simulation case 1, first simulation: steady-state heat fluxes

In these simulations, the sublimation power is initially neglected. However, it can be taken into account using the following iterative method:

1. Considering the initial simulation results, additional simulations can be performed considering the temperature inside the propellant. Since the pressure inside the tank is very close to the vapor pressure at low flow rates, as previously mentioned, the mass flow rate can be estimated using Equation 4.6 for the orifice diameter equal to 0.8 mm, assuming the tank pressure equals the vapor pressure.
2. From the mass flow rate, the power required for sublimation can be calculated

using the sublimation enthalpy (71 kJ/mol for naphthalene [20]), the flow rate, and the molecular mass:

$$\Delta P = \frac{\Delta H}{M\dot{m}} \tag{6.2}$$

3. Then another simulation can be carried out by applying a power equal to $4\ W - \Delta P$.

4. From this new simulation, the same steps are repeated, iterating until the temperature difference between successive iterations is less than 0.1 °C.

The convergence of the iteration for this case is shown in Figure 6.5. In the end, both the sublimation power and the resulting mass flow rate can be obtained for the given heat load configuration:

- **Real temperature inside the propellant**: 74.1 °C
- **Flow rate**: 0.880 mg/s
- **Sublimation power**: 0.489 W

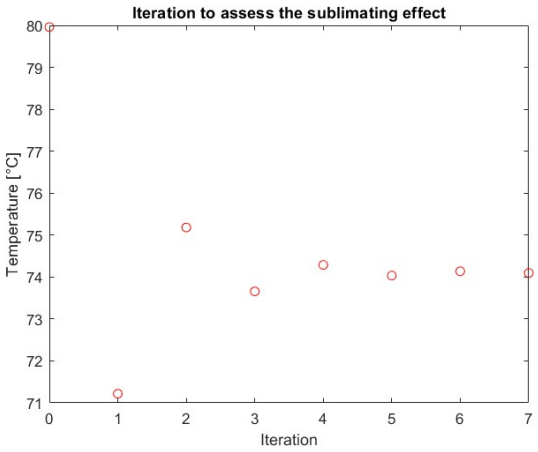

Figure 6.5: Iterations to assess the sublimation effect

Double orifice heaters power

Figure 6.6 presents the transient behavior resulting from doubling the orifice heaters power. It is evident that the temperatures of the tank and propellant are not affected by the heaters along the orifice, while the PCB farther from it is partially influenced.

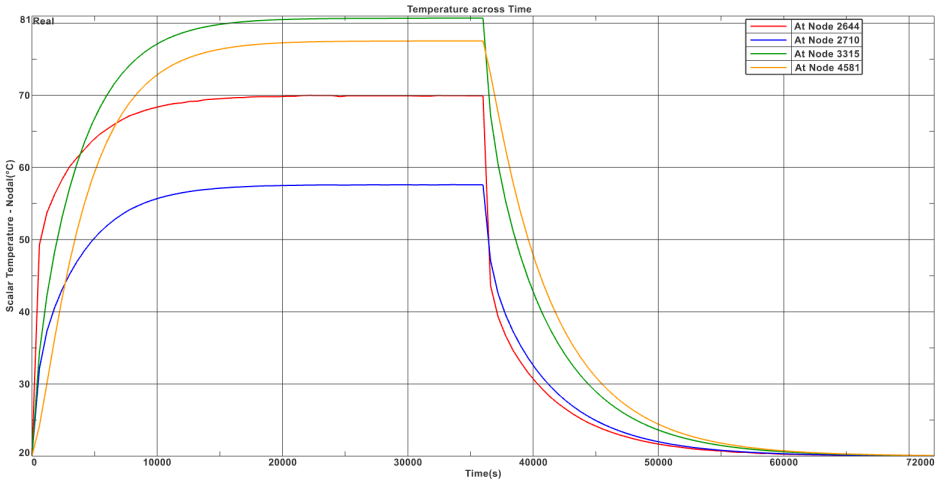

Figure 6.6: Thermal simulation case 1, first simulation with double power along the orifice: transient response

Half-filled tank

An additional simulation was conducted with the tank half full (Figures 6.7 and 6.8) to observe its impact on temperature distribution and thermal inertia throughout the system. In this case, the propellant temperature is slightly lower, and the steady state is reached faster.

These results show that the reduction in propellant volume does not significantly affect the performance of the thermal control system and would improve the thermal inertia.

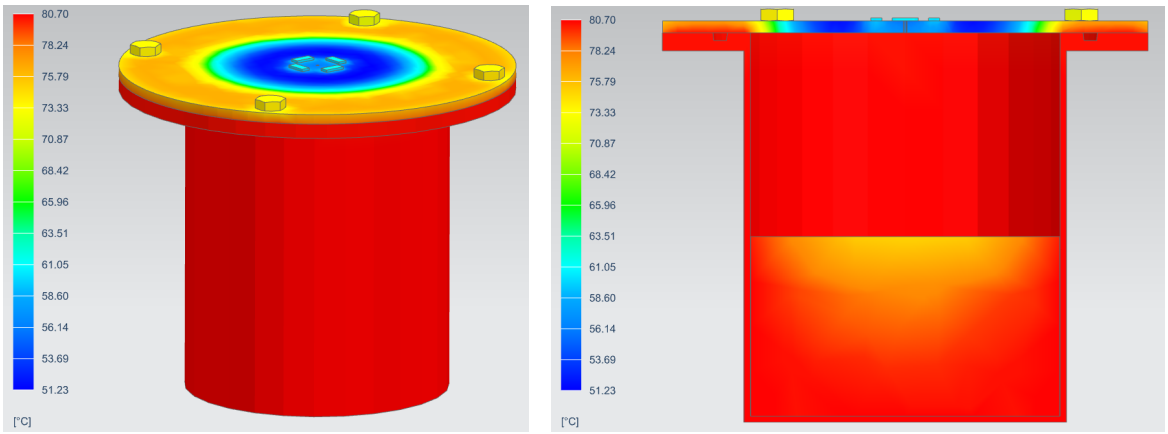

(a) Entire assembly (b) Section

Figure 6.7: Thermal simulation case 1, first simulation with half-filled tank: steady-state temperatures

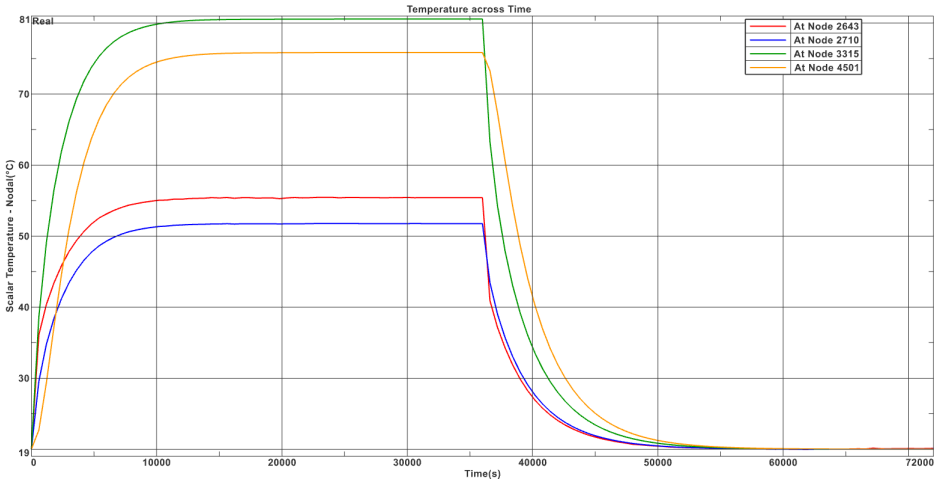

Figure 6.8: Thermal simulation case 1, first simulation with half-filled tank: transient response

6.5.2 Second simulation

Considering a lower heat input, the temperatures drop as illustrated in Figures 6.9 and 6.10.

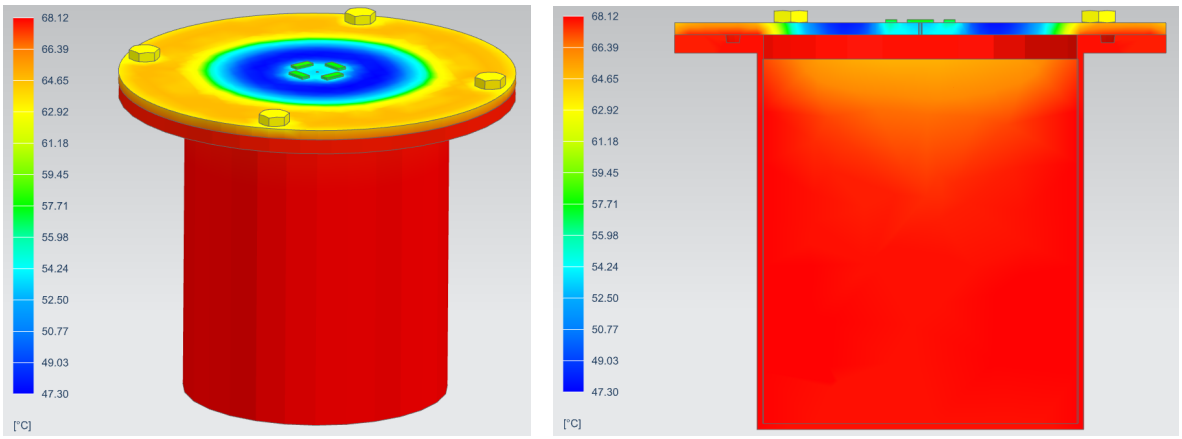

(a) Entire assembly (b) Section

Figure 6.9: Thermal simulation case 1, second simulation: steady-state temperatures

Accounting for the sublimation effect:

- **Real temperature inside the propellant**: 65.4 °C
- **Flow rate**: 0.446 mg/s
- **Sublimation power**: 0.246 W

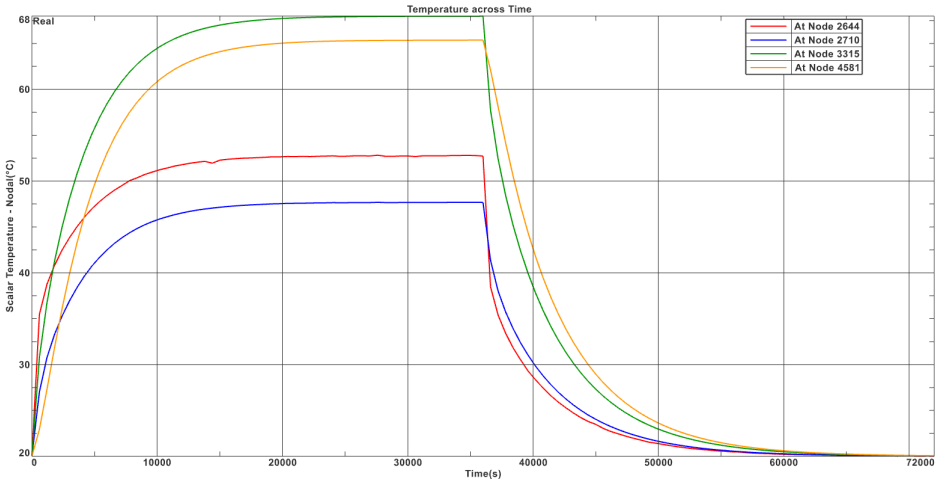

Figure 6.10: Thermal simulation case 1, second simulation: transient response

6.5.3 Third simulation

Figures 6.11 and 6.12 present the simulation results for a heat power of 2 W applied to the tank.

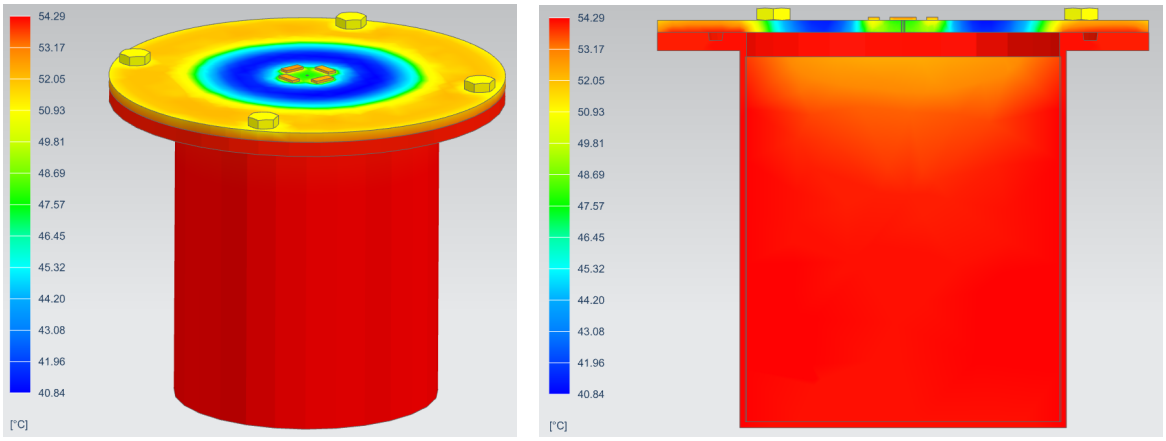

(a) Entire assembly (b) Section

Figure 6.11: Thermal simulation case 1, third simulation: steady-state temperatures

Accounting for the sublimation effect:

- **Real temperature inside the propellant**: 52.6 °C
- **Flow rate**: 0.181 mg/s
- **Sublimation power**: 0.100 W

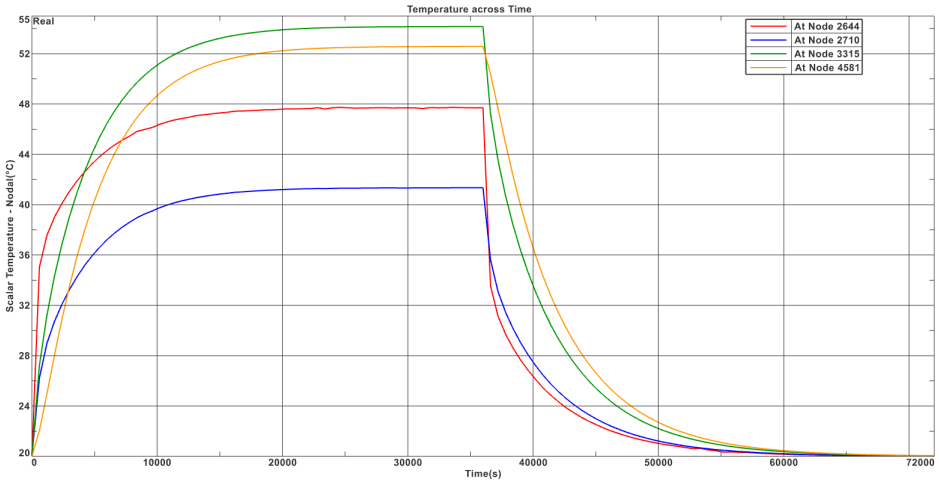

Figure 6.12: Thermal simulation case 1, third simulation: transient response

6.5.4 Fourth simulation

In the final simulation (Figures 6.13 and 6.14), the temperature of the propellant is approximately 38 degrees.

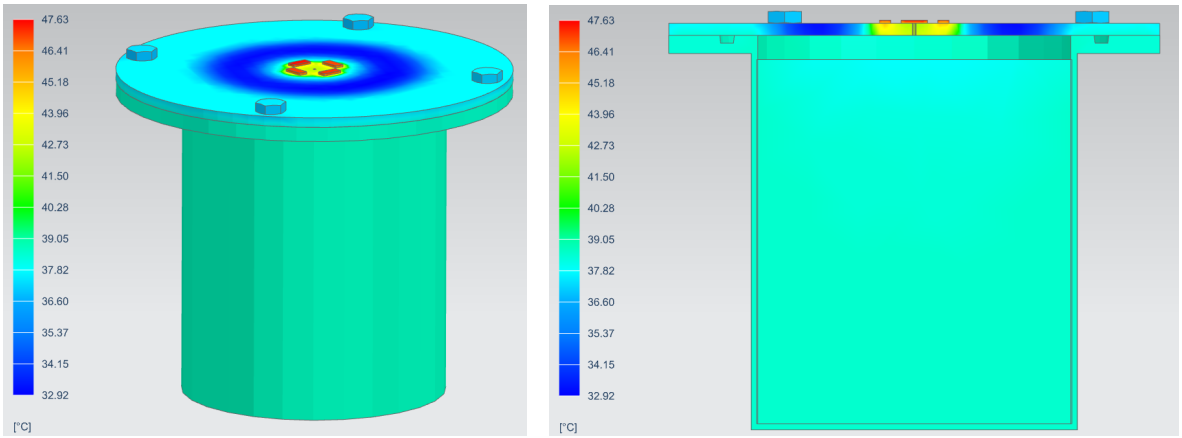

(a) Entire assembly (b) Section

Figure 6.13: Thermal simulation case 1, fourth simulation: steady-state temperatures

Accounting for the sublimation effect:

- **Real temperature inside the propellant**: 38.1 °C
- **Flow rate**: 0.0539 mg/s
- **Sublimation power**: 0.0298 W

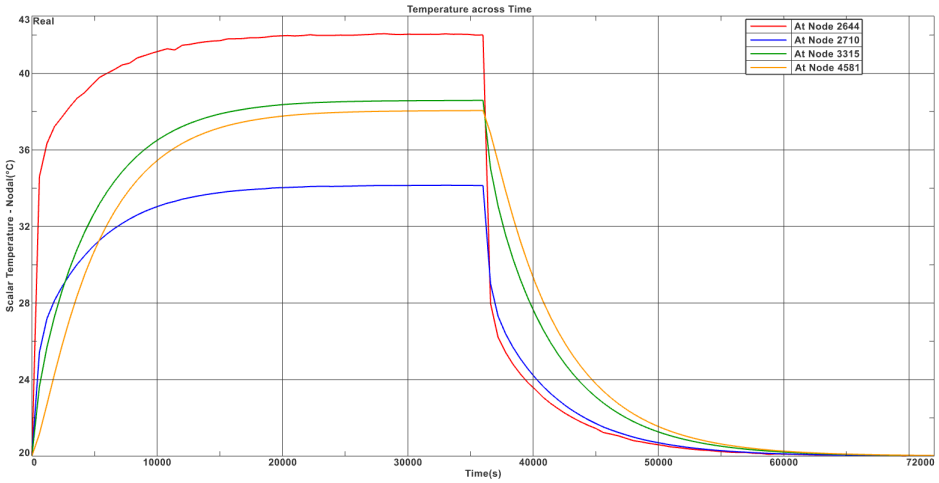

Figure 6.14: Thermal simulation case 1, fourth simulation: transient response

6.5.5 Steady-state plot

Keeping the same heat load on the orifice, steady-state simulations were carried out by varying the heat load applied to the tank. In Figure 6.15, the plot indicates the dependence of the orifice and internal propellant temperatures on different heating powers around the tank.

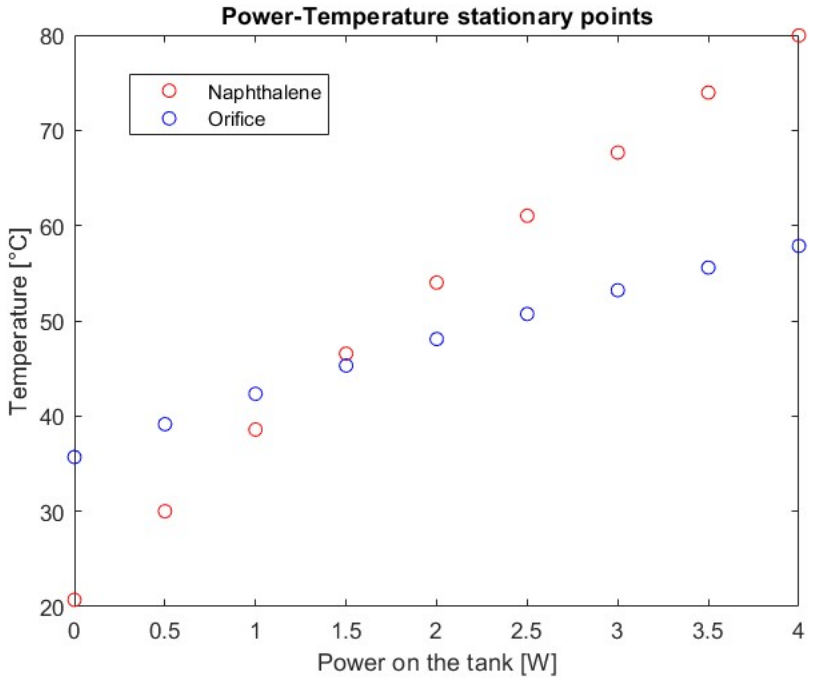

Figure 6.15: Thermal simulation case 1: temperature stationary points by changing the load on the tank

The orifice is only partially thermally decoupled from the tank. The tank, on the other hand, as shown at the lowest point of the graph, is not significantly affected by the

heating or cooling of the orifice, since the propellant temperature remains very close to the ambient temperature when no power is applied on the tank.

6.5.6 Considerations

This first case was useful for validating the design used in the final test. The temperature distribution along the system is as expected. The tank warms the propellant; instead, for the PCB this happens only along the contact surfaces. The temperature on the top surface of the propellant is slightly lower because of radiation exchanges with the lid.
It is also important to focus on the transient behavior: at first glance, such a large thermal inertia may appear unrealistic. A quick verification can be performed using the specific heat formula for the temperature derivative:

$$\frac{dT}{dt} = \frac{P}{mc} \tag{6.3}$$

This expression underestimates the transient time, as it neglects both conduction and radiative losses. It can be applied in an idealized scenario in which only the propellant is present and heated, with no thermal exchange with the surrounding environment. For this reason, it leads to an overestimation of the temperature increase rate: in such a case, the temperature would rise linearly over time without stabilization. However, the purpose of using this equation is to compare its ideal prediction with the simulation results. If the time scales are comparable, it suggests that the transient behavior in the simulation is physically reasonable.
Considering the first simulation, with a heating power of 4 W and a propellant mass of 0.145 kg, the temperature rate of change would be:

$$\frac{dT}{dt} \approx 0.02 \text{ K/s}$$

This implies that increasing the temperature from 20 to 80 degrees Celsius would require:

$$\Delta t = \frac{\Delta T}{\frac{dT}{dt}} \approx 50 \text{ min}$$

As can be seen, the estimated time magnitude is reasonable considering the initial temperature increase in Figure 6.3. The tank mass should also be included in Equation 6.3, which would result in values even closer to the ones of the simulation.

6.6 Case 2

For this case, MLI was integrated into the design; Figure 6.16 shows the simulated configuration. However, in the result images, MLI is omitted to improve clarity.

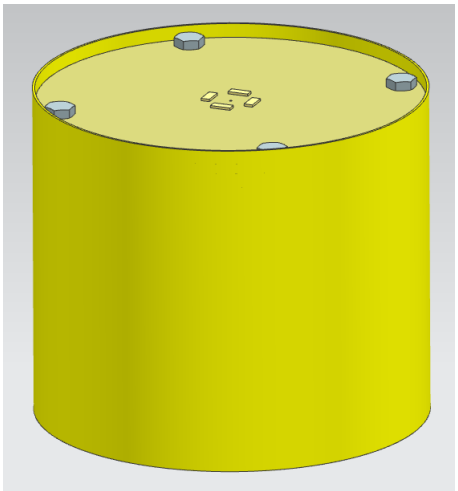

Figure 6.16: MLI integrated into the CAD model

Table 6.4 shows the correspondence between the nodes and their labels in the transient plot.

Node	Physical point
4485	Side surface of the tank
5751	Naphthalene top surface
2385	Orifice
2709	Point on the PCB far from the orifice and tank

Table 6.4: Thermal simulation case 2: nodes reported in the transient plots

6.6.1 First simulation

The thermal evolution, from steady-state temperature distribution to transient response, is detailed in Figures 6.17 and 6.18.
When using MLI, the temperature is higher and the warm-up transient is improved, while the cool-down transient is slower. This behavior is consistent with expectations.

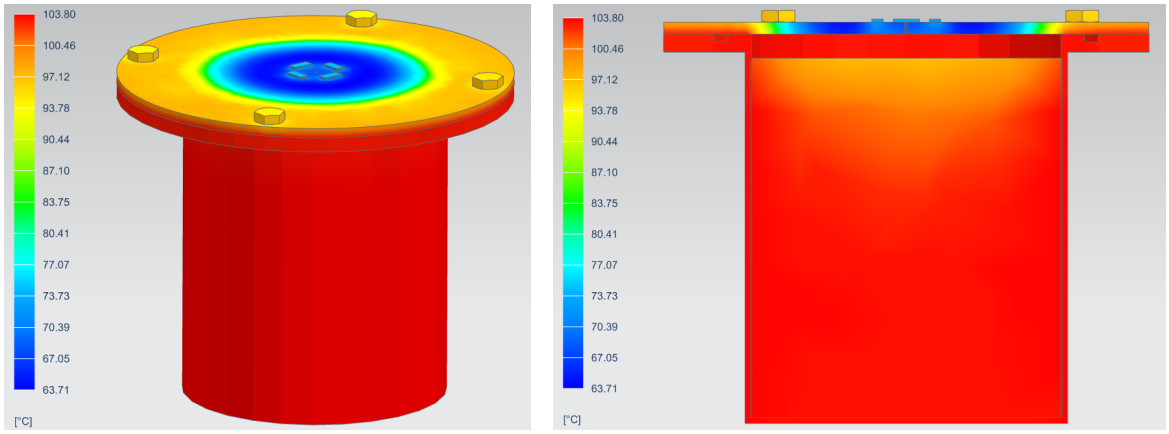

(a) Entire assembly (b) Section

Figure 6.17: Thermal simulation case 2, first simulation: steady-state temperatures

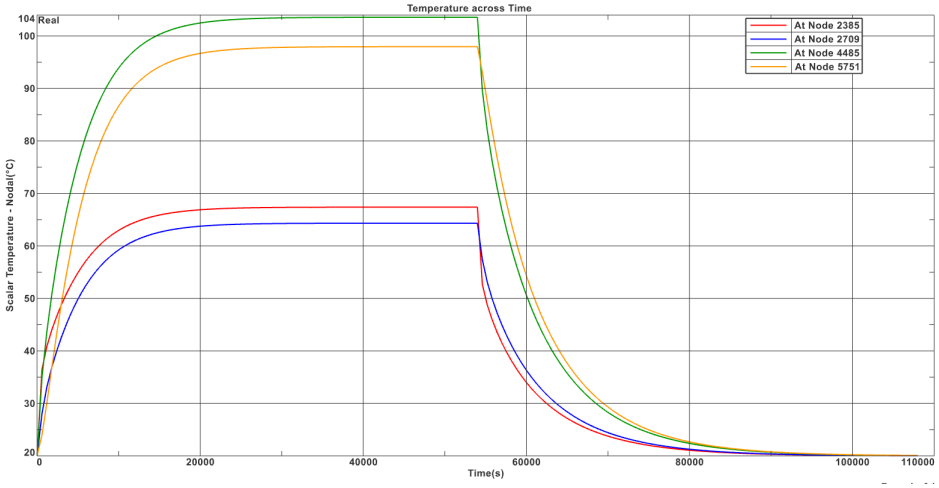

Figure 6.18: Thermal simulation case 2, first simulation: transient response

The sublimation effect was not included in this simulation due to the large number of iterations required.

6.6.2 Second simulation

A reduction in heat input leads to lower temperature (Figures 6.19 and 6.20). Accounting for the sublimation effect:

- **Real temperature inside the propellant**: 76.5 °C
- **Flow rate**: 1.04 mg/s
- **Sublimation power**: 0.570 W

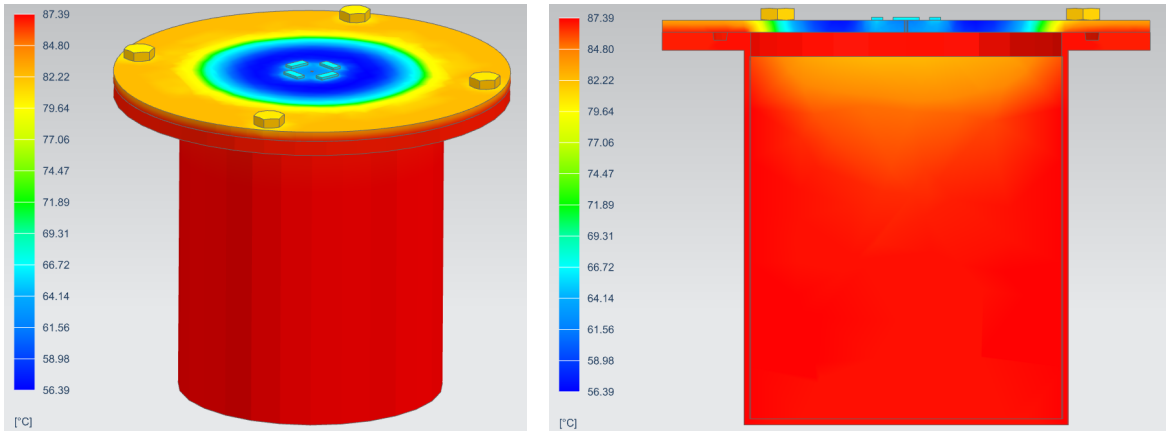

(a) Entire assembly (b) Section

Figure 6.19: Thermal simulation case 2, second simulation: steady-state temperatures

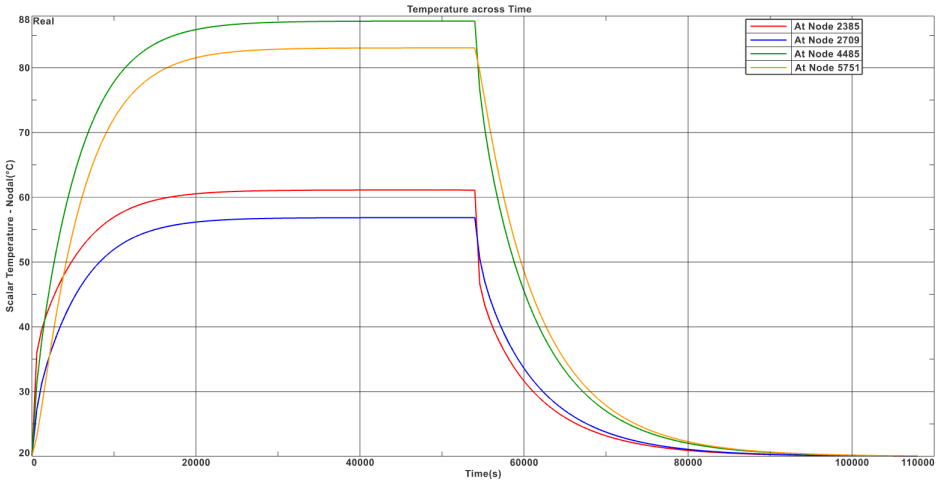

Figure 6.20: Thermal simulation case 2, second simulation: transient response

6.6.3 Third simulation

Figures 6.21 and 6.22 present the simulation results obtained with a heat input of 2 W applied to the tank.
Accounting for the sublimation effect:

- **Real temperature inside the propellant**: 63.6 °C
- **Flow rate**: 0.421 mg/s
- **Sublimation power**: 0.235 W

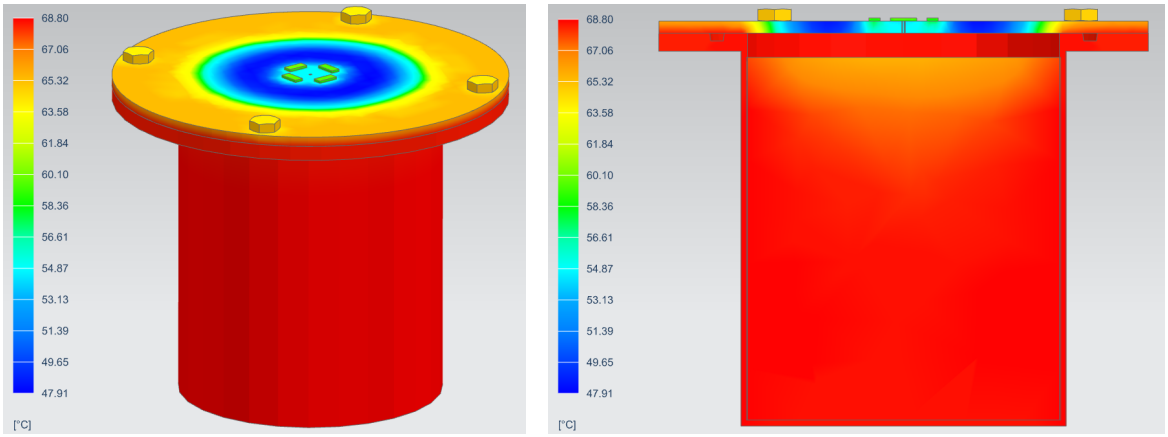

(a) Entire assembly (b) Section

Figure 6.21: Thermal simulation case 2, third simulation: steady-state temperatures

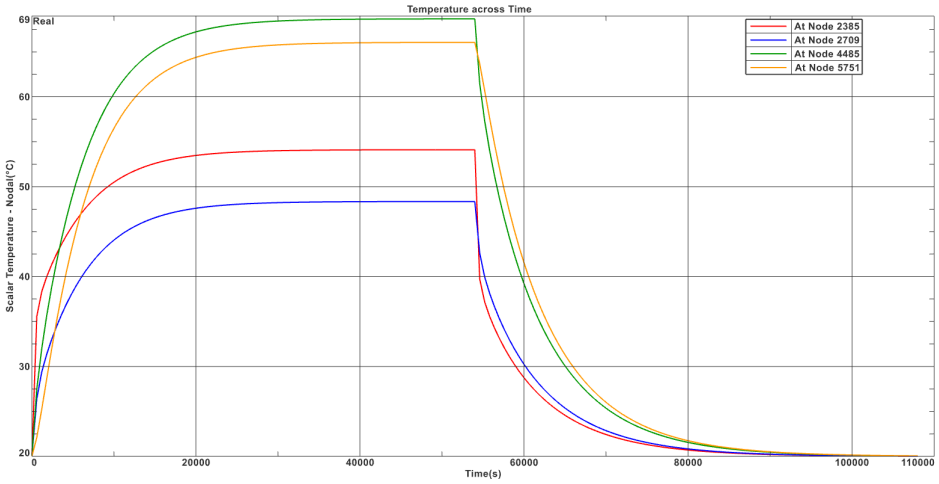

Figure 6.22: Thermal simulation case 2, third simulation: transient response

6.6.4 Fourth simulation

The final simulation (Figures 6.23 and 6.24) results in a propellant temperature of approximately 46 °C.
Accounting for the sublimation effect:

- **Real temperature inside the propellant**: 45.7 °C
- **Flow rate**: 0.103 mg/s
- **Sublimation power**: 0.0573 W

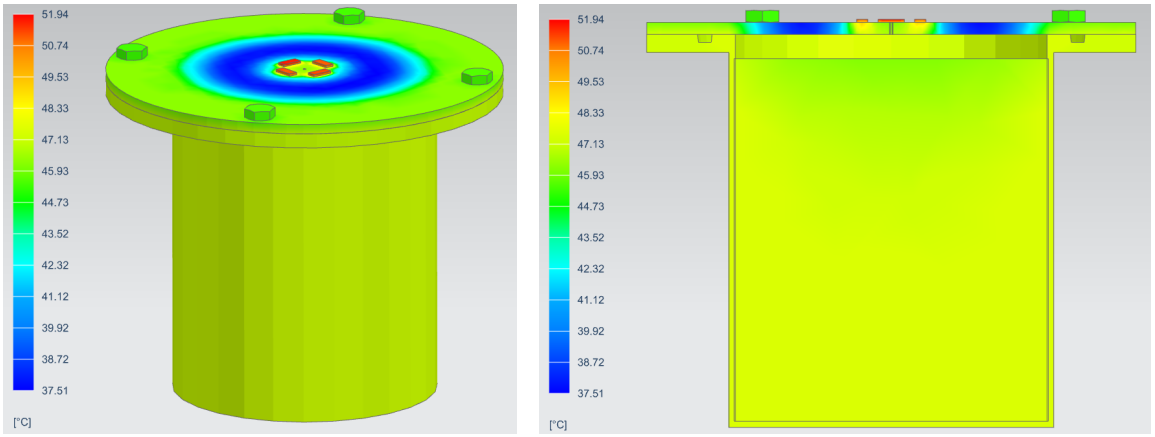

(a) Entire assembly (b) Section

Figure 6.23: Thermal simulation case 2, fourth simulation: steady-state temperatures

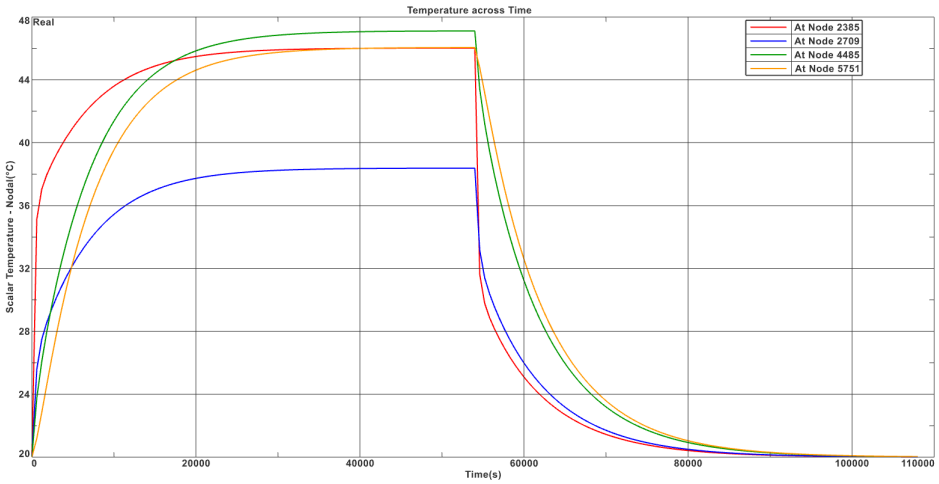

Figure 6.24: Thermal simulation case 2, fourth simulation: transient response

6.6.5 Steady-state plots

As in the previous case, steady-state simulations were performed by changing the heat load applied to the tank while keeping the heat load on the orifice constant, in order to observe the temperature trend (Figure 6.25).
It confirms what it was discussed about the orifice decoupling.

6.7 Takeaways and observations

The simulations highlighted both the system's performance and its limitations. The most significant issue observed is thermal inertia: although the use of MLI improves the warm-up time, the cool-down phase remains problematic. A partial solution could involve clogging the orifice to interrupt the flow when the thruster is turned off; this

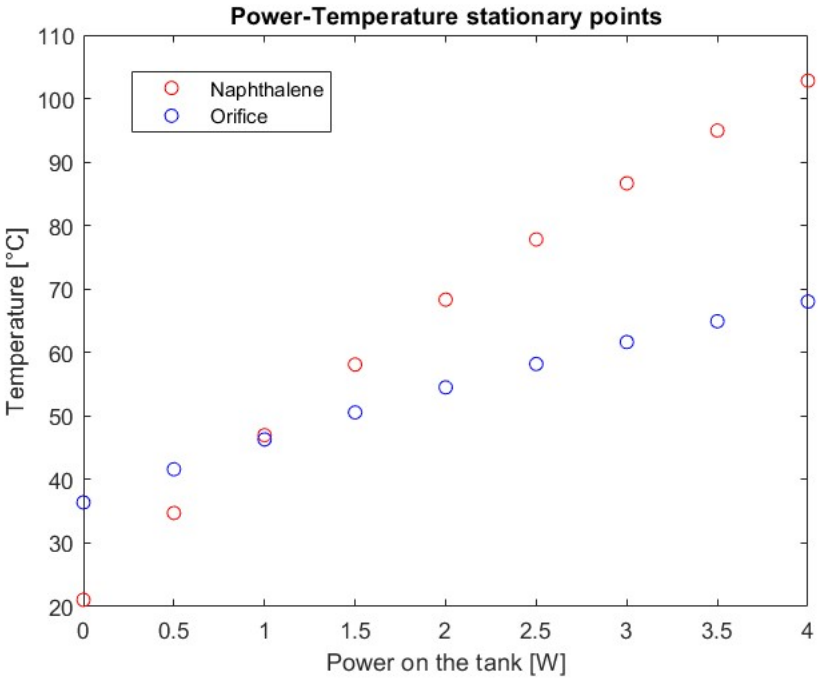

Figure 6.25: Thermal simulation case 2: temperature stationary points by changing the load on the tank

approach is evaluated during the final test campaign.

Another strategy to enhance transient behavior and reduce warm-up time is boosting the input power, as demonstrated in the preliminary tests. This solution is investigated in the final tests as well. In preparation for these tests, an additional simulation was performed by applying the thermal load beneath the tank rather than laterally, in order to assess whether the component's thermal conductivity is sufficient to ensure effective heating even with differently positioned heaters. The results confirm that both the temperature and its distribution remain nearly unchanged.

Table 6.5 summarizes the key simulation results obtained from the simulations with different heat loads applied to the tank, including the propellant temperature, the corresponding flow rate and the sublimation power. As shown, the achievable flow rate is satisfactory, and values up to 0.5 mg/s can be reached with a moderate power increase and without requiring excessively high temperatures.

	Propellant temperature [°C]	Flow rate [mg/s]	Sublimation power [W]
Case 1, 4 W applied	74.1	0.880	0.489
Case 1, 3 W applied	65.4	0.446	0.246
Case 1, 2 W applied	52.6	0.181	0.100
Case 1, 1 W applied	38.1	0.0539	0.0298
Case 2, 3 W applied	76.5	1.04	0.570
Case 2, 2 W applied	63.6	0.421	0.235
Case 2, 1 W applied	45.7	0.103	0.0573

Table 6.5: Key results from the simulations, with orifice heaters power equal to 0.005 W/mm^3

The final step is now to validate the key results (temperature and flow rate) through the final tests. These tests will confirm or refute our theoretical flow modeling and thermal simulations.

Chapter 7

Final tests

This chapter focuses on the final tests, comparing the experimental results with the theoretical predictions. The tests are carried out similarly to the preliminary ones, but without MLI.
The main system tested used the PCB with a 0.8 mm orifice diameter, as it was the first one delivered and includes the heating system modeled in the simulation. For the 0.6 mm orifice, only a few points were measured to evaluate the temperature distribution and the impact of orifice size on flow rate and clogging. This second PCB also has the heaters and the thermistor positioned closer to the orifice (in this way it is possible to glue the pipe), influencing the temperature distribution in that region, while the tank temperature should remain almost entirely unaffected due to the thermal decoupling. Due to malfunctions in the pressure sensor, it was not possible to activate the high-vacuum pump, as it requires low pressure and this variable could not be measured. As a result, only the rough pump was used, limiting the minimum achievable pressure inside the chamber to around 0.5–1 mbar. This affects the lower flow rate measurements, as the orifice may not be choked, making the results less reliable.

7.1 Components

Figure 7.1 shows the tank and the complete system. The system also includes the pipe; however, it is not used in the current configuration. Future work could test the system integrated with the pipe.

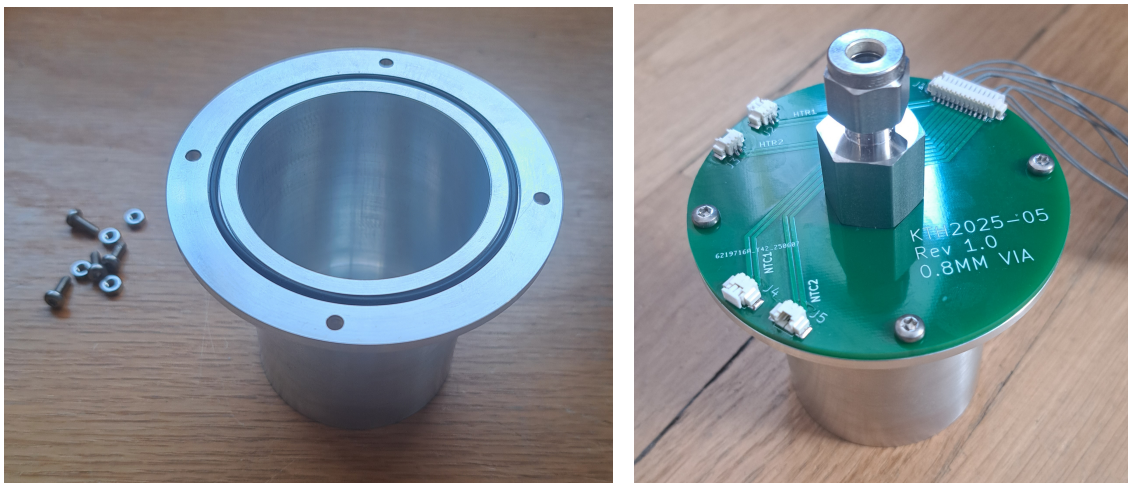

(a) Tank (b) Entire system

Figure 7.1: Pictures of the tank and the designed system

7.2 Experimental setup

The thermal control system is shown in Figure 7.2. It includes a NTC thermistor on the orifice (model ERTJ1VG103JA by Parasonic [23]) and a NTC thermistor probe on the tank (model 10K3MCD1 by TE Connectivity [30]), along with two separate heating systems.

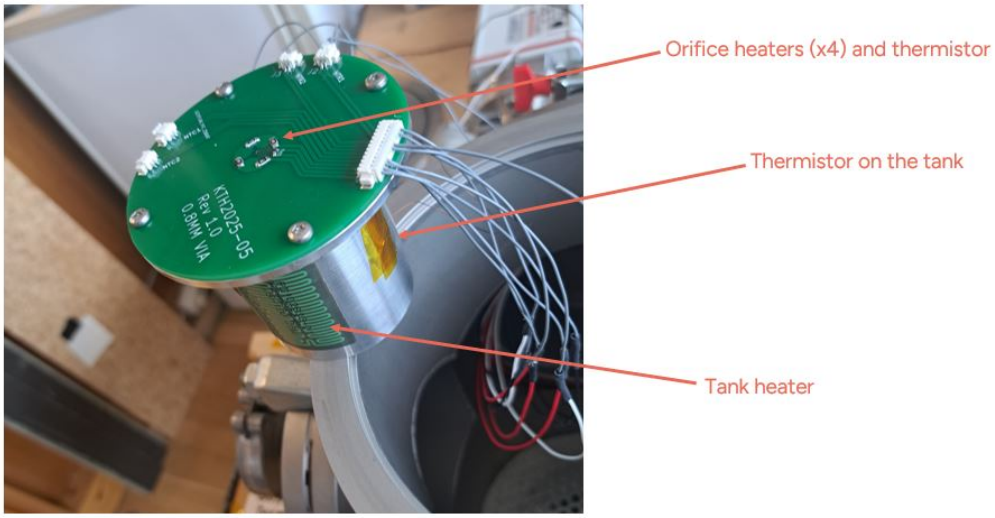

Figure 7.2: Thermal control system of the designed system

To avoid conductive losses to the chamber, the system was placed on a small plastic support (Figure 7.3).

Due to safety concerns, naphthalene vapors were vented outside the window through a pipe connected to the chamber pump (Figure 7.4). The connections were sealed with a plastic bag and plastic clamps.

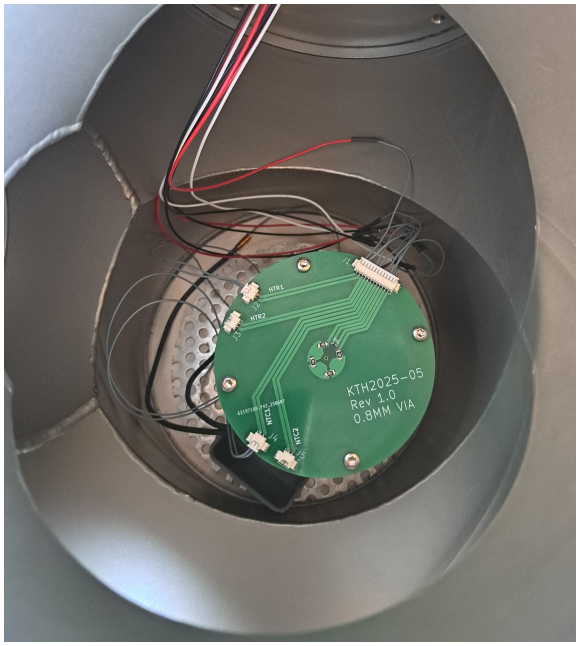

Figure 7.3: System tested inside the vacuum chamber

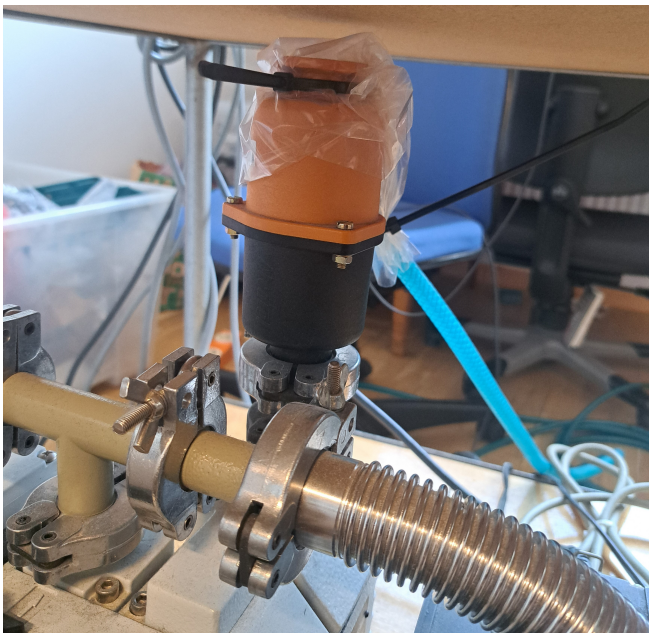

Figure 7.4: System to blow naphthalene vapors outside the window

The NTC thermistors are characterized by Equation 5.1, as observed in the preliminary tests. The corresponding Beta factors are:

- For the thermistor on the tank: $\beta = 3976\ K$
- For the thermistor on the orifice: $\beta_{25/50} = 3380$ K and $\beta_{25/85} = 3435$ K, depending on the temperature range. For temperatures up to 50 °C, the first one is preferable, while the second is more reliable at higher temperatures.

In Figure 7.5, the curves for the two different thermistors are shown.

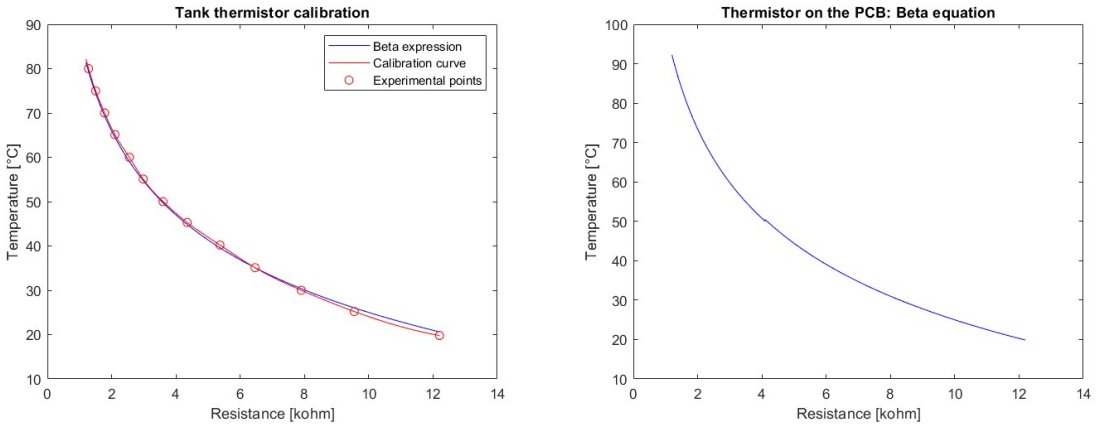

(a) Tank thermistor (b) PCB thermistor

Figure 7.5: Resistance-temperature plot of the thermistors used in the final tests

The tank thermistor was calibrated, while for the thermistor on the PCB it was not possible to calibrate it separately. For this reason, due to the long stabilization times for the PCB temperature and temperature oscillations in the thermal chamber, it was chosen to rely on the Beta expression.

7.3 Temperature and flow rate tests

Following the approach used in the preliminary tests, two types of experiments were conducted: tank heating with and without propellant. This enables analysis of the temperature distribution and achievable flow rates for both PCB configurations.
In Appendix B all the data from the tests are reported.

7.3.1 PCB with 0.8 mm of orifice diameter

Figure 7.6 shows the results of the tank warming tests. The plot reports the corresponding tank and orifice temperatures under different levels of heating power applied to the tank, with a fixed orifice heater power of 0.152 W (which means approximately 0.038 W for each heater). The value was deliberately chosen to be higher than that used in the simulation, both to reduce the risk of naphthalene condensation and to compensate for the simplification of modeling the orifice heaters as uniformly distributed.
The thermal inertia remained significant, as observed in the preliminary tests. Each

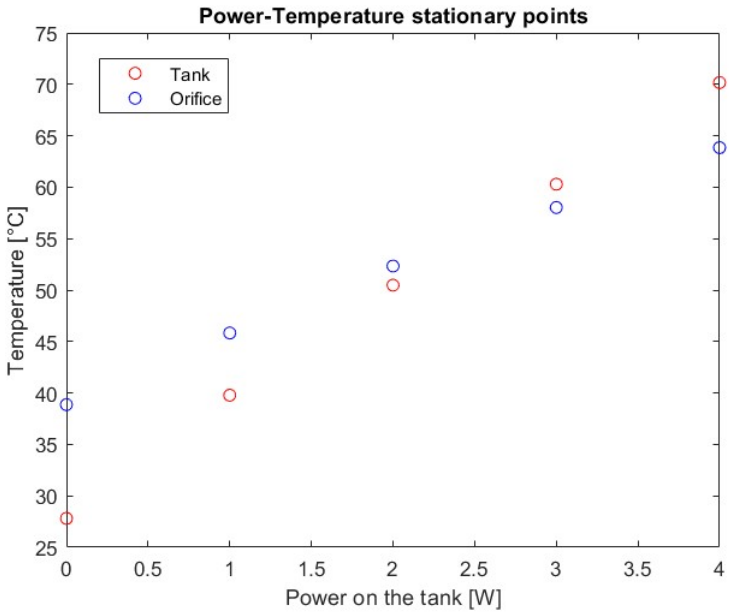

Figure 7.6: Power-temperature stationary points for the tank warming tests - PCB with 0.8 mm of orifice diameter

point was accelerated using a boosting phase, and two such tests were performed, one for the orifice heaters and one for the tank heaters. The results are as follows:

- The orifice can be easily boosted: for example, when no power is applied to the tank, applying a total power of 0.23 W to the orifice heaters allows the temperature to reach within 1-2 °C of the steady-state value in just 3 minutes.
- The tank can reach 70 °C in 7 minutes by applying 10 W of power, with the orifice heaters also active.

Additionally, the cool-down test starting from the highest temperature point showed a drop from 70 °C to 38 °C in 45 minutes, followed by more than 5 hours to bring the system back to ambient temperature.

A similar thermal inertia was observed with the propellant inside the tank. The corresponding results for temperature and flow rate are shown in Figure 7.7, with the same orifice power. Figure 7.8 provides a comparison with the tank-only warming tests. For the warmest point in the propellant tests, stabilization was not awaited in order to avoid depleting the propellant. As a result, the actual steady-state temperatures at that point are expected to be even higher than those recorded.

The flow rate was measured using Equation 5.2, based on the mass difference of the propellant before and after the test, and the corresponding elapsed time. The vacuum pump was activated when the temperature was already near its steady-state value,

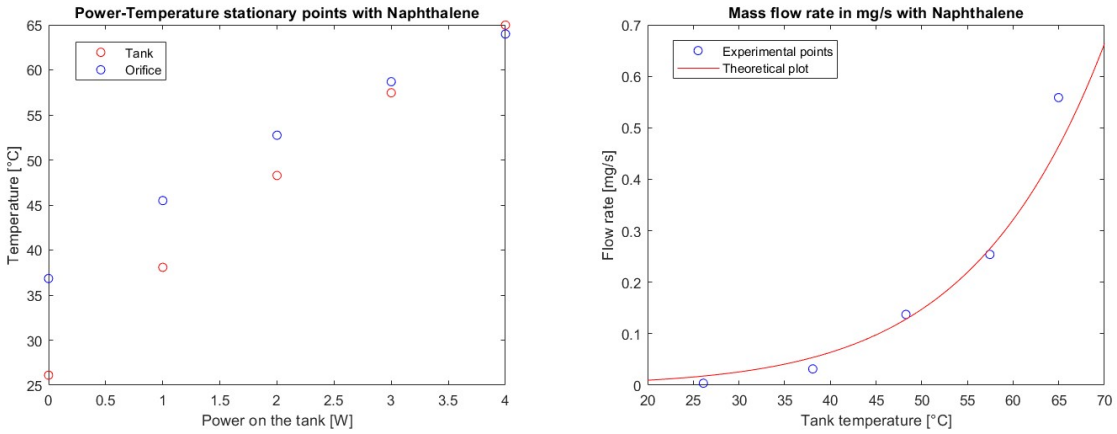

(a) Power-temperature plot (b) Temperature-flow rate plot

Figure 7.7: Propellant tests - PCB with 0.8 mm of orifice diameter

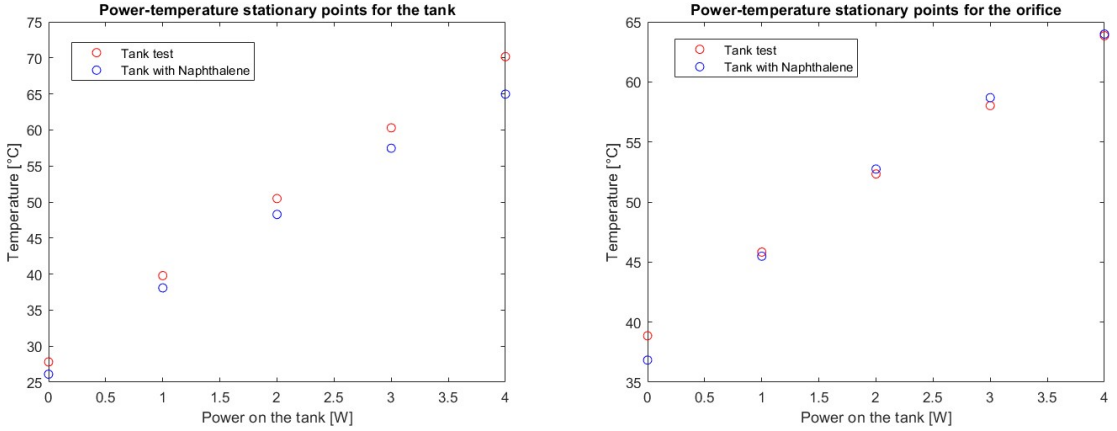

(a) Tank (b) Orifice

Figure 7.8: Comparison between tank warming and propellant tests - PCB with 0.8 mm of orifice diameter

to obtain a more accurate measurement of the flow rate corresponding to the stable temperature.

7.3.2 PCB with 0.6 mm of orifice diameter

The PCB with the smallest orifice features a different heating control system, with the heaters and thermistors located closer to the orifice (Figure 7.9, while the other one is visible in Figure 7.3). This is the most efficient way to heat the orifice while reducing power consumption, and the temperature measurement is more reliable since the thermistor is located closer to it.

Only two test points were performed with this system, both with and without the propellant. The results are shown in Figure 7.10 for the tank warming tests and in

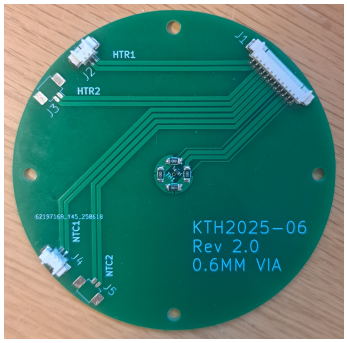

Figure 7.9: PCB with the smallest orifice

Figure 7.11 for the tests with propellant. Due to issues with the electrical connections, the orifice temperature could not be measured during the test without naphthalene. As a result, only the tank temperature could be compared between the two test types, as shown in Figure 7.12.

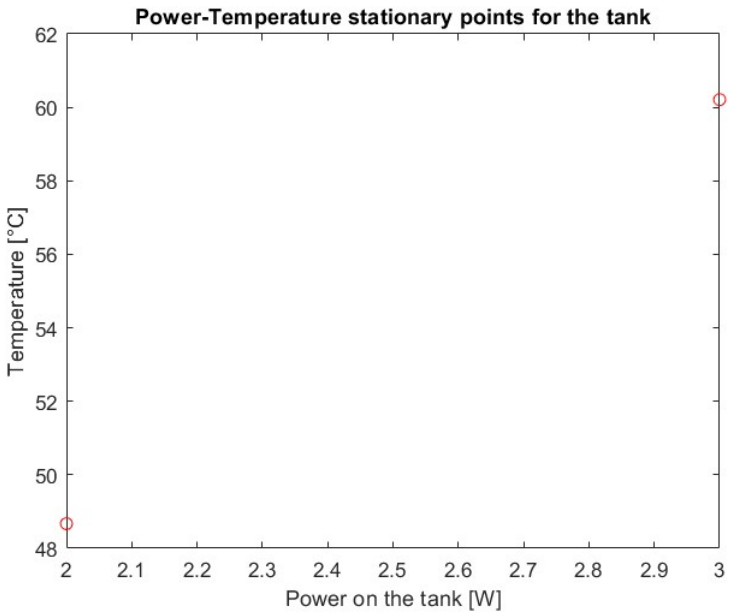

Figure 7.10: Power-temperature stationary points for the tank warming tests - PCB with 0.6 mm of orifice diameter

7.4 Clogging tests

Clogging tests were carried out on both PCBs, under three different conditions after the tank temperature was boosted close to its steady-state value:

1. No power on the orifice and 4 W applied to the tank from the beginning, for one hour.

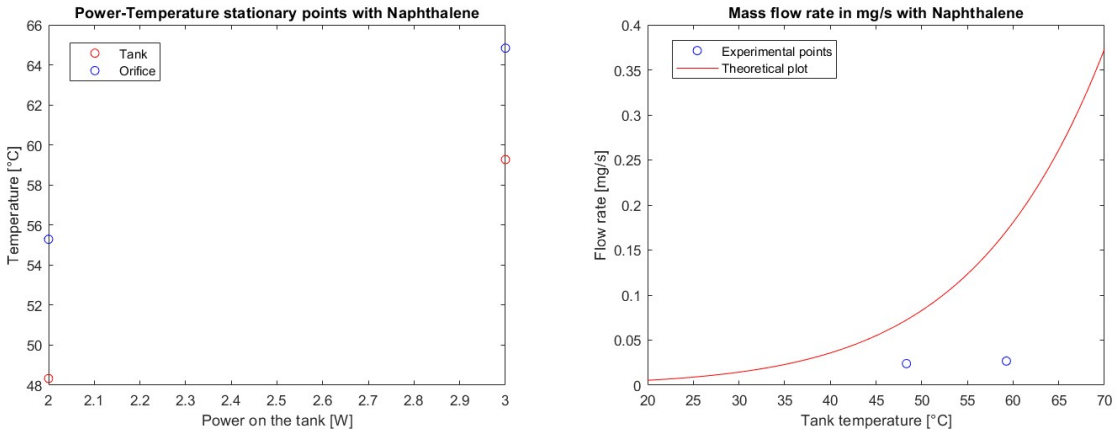

(a) Power-temperature plot (b) Temperature-flow rate plot

Figure 7.11: Propellant tests - PCB with 0.6 mm of orifice diameter

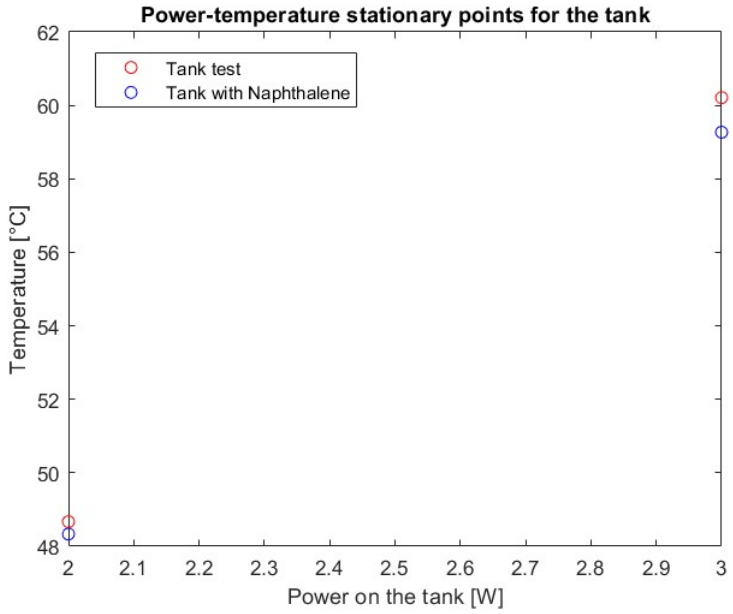

Figure 7.12: Comparison between tank warming and propellant tests - PCB with 0.6 mm of orifice diameter

2. The orifice was initially powered and a power of 4 W was applied to the tank, as set during the previous tests. Afterward, the orifice power was turned off for 20-30 minutes and then also the tank power to see if clogging could occur during the cooling phase. This phase was not entirely performed, but only for a duration of 15 minutes.

3. Same test as before, but with 2 W applied to the tank.

The most notable result was observed in the last two tests using the PCB with a 0.6 mm orifice diameter. Figure 7.13 shows the system after removal from the vacuum

chamber following the third test. As visible in the image, partial clogging occurred in a time frame significantly shorter than that required for the cooling phase. This suggests that clogging may have been triggered intentionally and, more importantly, that it could also occur under normal operating conditions.

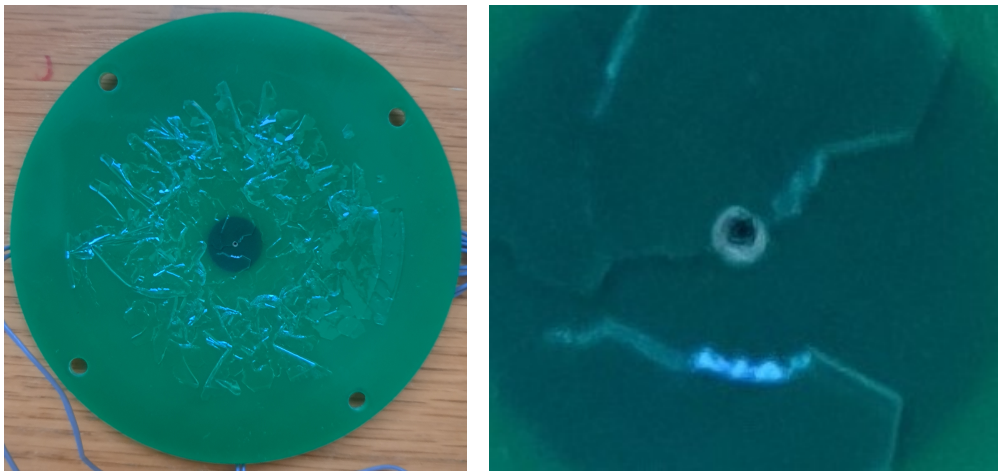

(a) Entire image (b) Zoom-in on the orifice

Figure 7.13: Clogging assessing on the PCB with 0.6 mm of orifice diameter

These results suggest that, for future work, it would be advisable to further investigate the clogging phenomenon. If clogging does not occur properly, a valve connected to the pipe could be considered to allow flow interruption when needed. Another potential approach could involve using multiple smaller orifices, where the likelihood of clogging may be higher.
Even the negative effects of clogging should be more thoroughly considered, as they could impact the flow rate during normal operation.

7.5 Drawbacks and uncertainties

Several drawbacks were encountered during the experiments:

- The chamber did not reach high vacuum, which adversely affected measurements at low flow rates. In addition, this caused naphthalene condensation inside the chamber (Figure 7.14), which further affected the internal pressure.
- Full stabilization required a long time, leading to some uncertainties and underestimations in the measurements of steady-state points.
- To weigh the naphthalene each time, it had to be placed in a separate container

Figure 7.14: Naphthalene condensation inside the chamber

due to the cables on the PCB and the tank, interfering with the balance reading. During this process, a small amount may have been lost.

- Electrical connections occasionally failed, necessitating repeated tests due to malfunctioning thermistors or heaters.
- The presence of cold spots on the PCB led to naphthalene condensation (Figure 7.15), which can influence the internal temperature of the system and, more critically, clog the orifice when it is small and the test duration is long. To partially mitigate this phenomenon, the power supplied to the orifice heaters can be further increased; however, the low thermal conductivity of the PCB would still result in the presence of cold spots.

(a) Entire image (b) Zoom-in on the orifice

Figure 7.15: Naphthalene condensation on the PCB during normal operation

These issues highlight areas for improvement in future test phases, such as the use of more robust electrical connections and a reliable pressure sensor.

7.6 Discussion

Discussing the results, the most remarkable finding is the capability of the PCB with an orifice diameter of 0.8 mm to deliver the required flow rate (more than 0.5 mg/s at 65 °C) with a power less than 4 W, as shown in Figure 7.7. The experimental points match the theoretical prediction very well, especially at high flow rates, where the discharge coefficient is expected to remain constant (Figure 4.3), confirming the validity and reliability of the developed model.
In contrast, the PCB with a 0.6 mm orifice diameter exhibited a significantly lower flow rate compared to theoretical expectations. Several factors may contribute to this discrepancy, including possible microscopic clogging of the orifice or a change in the flow regime as the orifice size decreases.
The Knudsen number is defined as the ratio between the mean free path λ of the gas molecules and a characteristic dimension L:

$$Kn = \frac{\lambda}{L} \tag{7.1}$$

This non-dimensional parameter determines the flow regime. When Kn > 0.01, the flow starts to become rarefied, requiring theoretical models different from those used in this work, and invalidating the assumptions of choked flow in the continuum regime. In the rarefied regime, continuous profiles of temperature and pressure no longer exist, and the mass flow rate is governed by molecular collisions.
In this case, L corresponds to the orifice diameter, which in the continuum regime is the main parameter controlling the flow rate. As L decreases, Kn increases. According to gas kinetic theory, the mean free path can be expressed as:

$$\lambda = \frac{k_B T}{\sqrt{2}\pi d^2 p} \tag{7.2}$$

where d is the mean molecular diameter, which for naphthalene is 6.2 Å [11].
To provide a conservative estimation, considering the two experimental points for the PCB with a 0.6 mm orifice diameter, and assuming a temperature of 50 °C and a pressure of 1 mbar (from Figure 3.7), the mean free path is equal to 26.1 μm. Given

a characteristic length of 0.6 mm, the resulting Knudsen number is equal to 0.0435. This shows that, for both PCBs, the flow may not be fully in the continuum regime, and that even a small reduction in orifice diameter pushes the system further into the rarefied regime. This effect may be a possible explanation for the discrepancy from the flow rate model observed during the preliminary tests for the 0.6 mm orifice case.

The two PCBs can be compared in terms of tank temperature: by examining Figures 7.6 and 7.10, it is evident that the measured temperatures are very similar. Figure 7.6 also highlights the thermal decoupling of the tank from the orifice, as expected. Additionally, for both PCBs, naphthalene condensation around the orifice and potential clogging were observed, which warrants further investigation. It is likely that, if the flow rate was achieved with the PCB featuring the smallest orifice, clogging would occur more easily.
The sublimation power can be assessed using Equation 5.3, the results are reported in Tables 7.1 and 7.2.

Flow rate [mg/s]	Sublimation power [W]
0.00380	0.00209
0.0316	0.0175
0.137	0.0761
0.254	0.141
0.559	0.309

Table 7.1: Sublimation power - PCB with 0.8 mm of orifice diameter

Flow rate [mg/s]	Sublimation power [W]
0.0239	0.0132
0.0267	0.0148

Table 7.2: Sublimation power - PCB with 0.6 mm of orifice diameter

These values, together with the external temperatures and the differences/inaccuracies in the experimental setups, influence the temperature differences observed between the tank warming tests and those conducted with the propellant. In addition, the condensation of naphthalene observed during the tests with the propellant contributes to an increase in temperature along the system.

By comparing Figure 7.7 with the simulation results (Figure 6.15 and Table 6.5), it is evident that the simulation tends to overestimate the tank temperature and underestimate the orifice temperature, particularly at higher power levels. This discrepancy is likely due to the limitations in modeling the orifice heaters and the chamber walls, as previously discussed.
Moreover, the experimental tests were carried out under configurations that were not fully replicated in the simulation, particularly regarding the amount of propellant loaded in the tank and its physical form (more powdered), as well as the presence of the plastic support, which was not included in the model. These factors, together with the

limitations encountered during the experiments, contributed to the deviations between the experimental and numerical results and indicate that not all tests were conducted under perfectly identical conditions. Additional discrepancies between the different experiments may also arise from slight variations in the position of the system inside the chamber or on the plastic support.

However, it can be stated that the simulation remains a valuable tool for providing an overall estimate of the temperatures involved, understanding the temperature distribution throughout the system, and, most importantly, evaluating the thermal inertia. The pipe could be integrated into the simulation model as part of future work, in order to gain preliminary insight into the system behavior prior to experimental testing.

Chapter 8

Conclusions and future work

In this chapter, based on the final tests, conclusions are drawn regarding the achievable flow rate and the developed theory and simulations. In addition, future work and potential improvements for both the system and the testing phase are discussed.

8.1 Conclusions

At the end, the main goal of the project was successfully achieved: the system design is capable of producing the required flow rate, reaching up to 0.5 mg/s at approximately 60°C using the PCB with a 0.8 mm orifice diameter. These results are remarked in Figure 8.1, which shows the temperature–flow rate plot with a logarithmic scale for the flow rate.

The monitoring of key variables was partially achieved: the temperature was successfully monitored, but the chamber pressure could not be measured due to sensor malfunctions. This highlights the need for proper pressure monitoring and high-vacuum conditions in future tests.

The PCB with a 0.8 mm orifice diameter proved to be the most advantageous configuration, as it produces higher flow rates. In contrast, the 0.6 mm orifice exhibited several drawbacks that rendered this configuration much less efficient. The results indicate that the optimal configuration is the system with a 0.8 mm orifice diameter, moving heaters and the thermistor closer to the orifice to enhance temperature monitoring and minimize power consumption.

Although the simulation model is not completely accurate for the temperature values, it provides valuable insight into the temperature distribution, thermal decoupling,

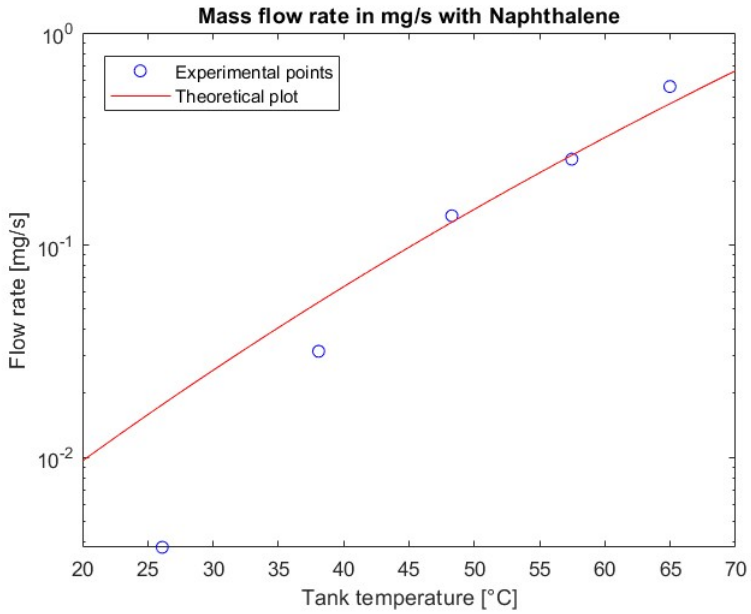

Figure 8.1: Obtainable flow rate for the PCB with 0.8 mm of orifice diameter

and system response time. It is also a useful tool for estimating the temperature corresponding to different heating power levels. Moreover, the flow model developed during the project was shown to be accurate and can serve as a predictive tool for future design iterations or similar systems.
Some limitations were encountered during the tests such as the slow thermal inertia, which made it difficult to precisely measure steady-state conditions, for example with the highest temperature point during the test with the propellant. However, flow-rate measurements can still be considered reasonably accurate, despite incomplete achievement of high vacuum, minor propellant losses during handling, and small temperature increases near stabilization.

8.2 Future work

Future work can include:

- Further investigate the PCB with the smallest orifice by performing additional and specific tests.
- Move and test the heaters and the thermistor closer to the orifice for the PCB with a 0.8 mm orifice diameter.
- Perform tests under high vacuum conditions and with a more optimized

experimental setup (as discussed in Section 7.5).

- Analyze the clogging behavior in more detail and, if the orifice cannot be blocked, integrate a valve to enable proper flow control when the thruster is off.
- Test the complete feeding system including the pipe and (eventually) the valve, confirming the expectations about the decoupling.
- Reduce mass and power consumption, for example, by using thermal insulators and evaluating performance improvements. Another way could be the use of different materials with lower emissivity (for example, high polished aluminum) to reduce radiative emissions and reduce power consumption.

At the thruster level, assessing the interaction between the feeding system and the thruster is crucial. Since the thruster is connected through the feed pipe, the interface may affect the temperature distribution within the tank and feed line, therefore influencing the flow rate. This effect must be evaluated, tested, and compensated for, even though the tank is expected to be partially thermally decoupled from the thruster. In addition to thermal aspects, tests on the thruster are required to confirm the validity of the flow rate model and the consistency of the flow rate magnitudes throughout the entire system.
What remains evident from this project is the potential of naphthalene as a propellant, provided that the necessary safety protocols are followed during system design and experimental validation.

Bibliography

[1] Ambrose, D. et al. “The vapour pressure of naphthalene”. In: *The Journal of Chemical Thermodynamics* (1975). DOI: https://doi.org/10.1016/0021-9614(75)90038-5.

[2] Apple Rubber. *ISO 3601 Metric Size O-Rings*. URL: https://www.applerubber.com/src/pdf/iso-3601-metric-size-o-rings.pdf.

[3] Backer Calesco. *STOCK FLEXIBLE FOIL HEATERS*. URL: https://www.backercalesco.com/download/18.37a02f9e180bfd9c6c74d6/1653038986686/Standard%20heater%20selection.pdf.

[4] Borrfors, André Nyberg et al. “Aromatic hydrocarbons as Molecular Propellants for Electric Propulsion Thrusters”. In: *Journal of Electric Propulsion* (2023). DOI: https://doi.org/10.1007/s44205-023-00059-6.

[5] Bretti, Michael A. “Progress and Developments of Ultra-Compact 10 Watt Class Adamantane Fueled Hall Thrusters for Picosatellites”. In: *37th International Electric Propulsion Conference (IEPC)*. IEPC-2022-349. 2022. URL: https://appliedionsystems.com/wp-content/uploads/2022/06/IEPC-2022-349.pdf.

[6] Bronkhorst. *LOW- ΔP-FLOW*. URL: https://www.insatech.com/media/53epndml/bu_e_low-dp-flow_bronkhorst.pdf.

[7] Dietz, Patrick et al. “Molecular propellants for ion thrusters”. In: *Plasma Sources Science and Technology* (2019). DOI: https://doi.org/10.1088/1361-6595/ab2c6c.

[8] Fowler, Lewis et al. “Vapor pressure of naphthalene. Measurements between 40.deg. and 180.deg.” In: *Journal of Chemical Engineering Data* (1968). DOI: https://doi.org/10.1021/je60037a020.

[9] Gorev, V. N. et al. “The effect of the PCB solder mask type of the hull outer surface of the CubeSat 3U on its thermal regime”. In: *IOP Conference Series: Materials Science and Engineering* (2020). DOI: https://doi.org/10.1088/1757-899X/734/1/012027.

[10] Hagstrom, Nathan P. et al. “Characterization of compressible flow through microscale orifice arrays”. In: *International Journal of Heat and Fluid Flow* (2023). DOI: https://doi.org/10.1016/j.ijheatfluidflow.2023.109173.

[11] Hu, Changsong et al. “Molecular shape selectivity of HZSM-5 in catalytic conversion of biomass pyrolysis vapors: The effective pore size”. In: *Energy Conversion and Management* (2020). DOI: https://doi.org/10.1016/j.enconman.2020.112678.

[12] Jobson, D. A. “On the Flow of a Compressible Fluid through Orifices”. In: *Journal of Mechanical Engineering Science* (1955). DOI: https://doi.org/10.1243/PIME_PROC_1955_169_077_02.

[13] L., Camin David and D., Rossini Frederick. “Physical Properties of Fourteen API Research Hydrocarbons, C9 to C15”. In: *The Journal of Physical Chemistry* (1955). DOI: https://doi.org/10.1021/j150533a014.

[14] Lee, Wen Yaung and Slutsky, L. J. “Heat of Vaporization, Infrared Spectrum, and Lattice Energy of Adamantane”. In: *The Journal of Physical Chemistry* (1975). DOI: https://doi.org/10.1021/j100591a007.

[15] Lengowski, Micheal. “Entwicklung mechanisch/thermischer Architekturen und innovativer Strukturelemente im Rahmen zweier Satellitenmissionen des Stuttgarter Kleinsatellitenprogramms”. Universität Stuttgart, 2013.

[16] Marcia L. Huber and Allan H. Harvey. *Viscosity of Gases*. URL: https://tsapps.nist.gov/publication/get_pdf.cfm?pub_id=907539.

[17] Martínez, J. Martínez and Rafalskyi, D. “Design and development of iodine flow control systems for miniaturized propulsion systems”. In: *CEAS Space Journal* (2021). DOI: https://doi.org/10.1007/s12567-021-00384-2.

[18] Merck. *Swagelok® Connector to Female NPT*. URL: https://www.sigmaaldrich.com/SE/en/product/supelco/22708.

[19] National Institute of Standards and Technology (NIST). *Adamantane*. URL: https://webbook.nist.gov/cgi/cbook.cgi?ID=C281232&Mask=4.

[20] National Institute of Standards and Technology (NIST). *Naphthalene*. URL: https://webbook.nist.gov/cgi/cbook.cgi?Source=1971RAD1310&Units=SI&Mask=1EFF.

[21] National Institute of Standards and Technology (NIST). *Pyrene*. URL: https://webbook.nist.gov/cgi/cbook.cgi?ID=C129000&Type=IR-SPEC&Index=2#IR-SPEC.

[22] Omega. *Low Pressure Drop Mass Gas Flow Controllers*. URL: https://br.omega.com/omegaFiles/green/pdf/FMA-LP2600A.pdf.

[23] Parasonic. *Multilayer NTC Thermistors ERTJ series*. URL: https://www.farnell.com/datasheets/4379317.pdf.

[24] Pfeiffer Vacuum. *HPT 100 Operating Instructions*. URL: https://fergutec.com/wp-content/uploads/2014/05/Pfeiffer-HPT-100.pdf.

[25] RS Components. *RS PRO Nitrile O-Ring O-Ring, 60.05mm Bore, 63.61mm Outer Diameter*. URL: https://se.rs-online.com/web/p/gaskets-o-rings/2562484?gb=s.

[26] SNS Insider. *Naphthalene Market*. URL: https://www.snsinsider.com/reports/naphthalene-market-5861.

[27] Snyder, John Steven et al. "Recommended Practice for Flow Control and Measurement in Electric Propulsion Testing". In: *Journal of Propulsion and Power* (2016). DOI: http://dx.doi.org/10.2514/1.B35644.

[28] Szabo, James et al. "Bismuth Vapor Hall Effect Thruster Performance and Plume Experiments". In: *35th International Electric Propulsion Conference Georgia Institute of Technology*. 2017.

[29] Szabo, James et al. "Performance Evaluation of an Iodine-Vapor Hall Thruster". In: *The Journal of Chemical Thermodynamics* (2012). DOI: https://doi.org/10.2514/1.B34291.

[30] TE Connectivity. *MICRO-BETACHIP (MCD) Thermistor Probe*. URL: https://www.farnell.com/datasheets/2305667.pdf.

[31] ThrustMe. *ThrustMe NPT30-I2 iodine electric propulsion system launched on board the NorSat-TD satellite*. URL: https://www.thrustme.fr/post/89-thrustme-npt30-i2-iodine-electric-propulsion-system-launched-on-board-the-norsat-td-satellite.

[32] Tirila, Vlad-George. “The Investigation of Alternative Solid Propellants in Hall Effect Thrusters”. PhD thesis. University of Southampton, 2024.

[33] Tirila, Vlad-George et al. “Zinc Propellant Storage and Delivery System for Hall Thrusters”. In: *AIAA Propulsion and Energy* (2021). DOI: https://doi.org/10.2514/6.2021-3407.

[34] Toukhy,
Mahmoud Ali Refaey El and Alsaydalani, Majed Omar. “INVESTIGATION OF THE DISCHARGE COEFFICIENT FOR ORIFICE AND PIPE BEHAVIOR”. In: *Journal of Engineering Science and Technology* (2022).

[35] Tsifakis, Dimitrios et al. “Naphthalene as a Cubesat Cold Gas Thruster Propellant”. In: *Frontiers in Physics* (2020). DOI: 10.3389/fphy.2020.00389.

[36] Vishay BCcomponents. *NTC Thermistors, Standard Lug Sensors*. URL: https://www.vishay.com/docs/29194/ntcalug54am5.pdf.

[37] Wikipedia. *Adamantane*. URL: https://en.wikipedia.org/wiki/Adamantane.

[38] Wu, Duqiang et al. “AN EMPIRICAL DISCHARGE COEFFICIENT MODEL FOR ORIFICE FLOW”. In: *International Journal of Fluid Power* (2002).

Appendix - Contents

Appendix A

Preliminary tests data

This appendix reports the measurement data of the preliminary tests. Although not measured during every test, the external temperature was consistently around 21.9 °C whenever it was recorded.

A.1 Tank tests

All raw data from preliminary tank tests without and with MLI are presented in Tables A.1 and A.2, including the date of the tests, the thermistor resistance measurements, and the power supply settings.

Test number	Date	Tank resistance [kΩ]	Current [A]	Voltage [V]
1	17/04/2025	11.9	0	0
2	18/04/2025	10.9	0.0990	0.420
3	18/04/2025	10.4	0.199	0.800
4	18/04/2025	9.65	0.300	1.24
5	18/04/2025	8.90	0.402	1.68
6	18/04/2025	8.05	0.502	2.10
7	18/04/2025	7.22	0.602	2.50
8	18/04/2025	6.24	0.702	2.94
9	19/04/2025	4.71	0.903	3.87
10	19/04/2025	4.05	1.00	4.36
11	19/04/2025	2.70	1.21	5.34

Table A.1: Raw data from the preliminary tank tests without MLI

Test number	Date	Tank resistance [kΩ]	Current [A]	Voltage [V]
1	11/05/2025	11.3	0	0
2	11/05/2025	9.56	0.0990	0.420
3	11/05/2025	7.81	0.199	0.800
4	12/05/2025	5.48	0.300	1.24
5	12/05/2025	3.97	0.402	1.68
6	12/05/2025	2.69	0.502	2.10

Table A.2: Raw data from the preliminary tank tests with MLI

A.2 Propellant tests

Table A.3 reports the data of the preliminary propellant tests, including the date and duration of the tests, the thermistor resistance measurements, and the initial and final mass (of the glass container with propellant inside). To optimize space, the power supply settings are not reported here, as they are the same as those of Table A.2.

Test n.	Date	Duration	Tank res. [kΩ]	Orifice res. [kΩ]	In. mass [g]	Final mass [g]
1	14/05/2025	16 h	11.4	11.4	12.35	12.30
2	15/05/2025	16 h	9.80	10.4	12.30	12.22
3	15/05/2025	16 h	8.24	9.62	11.50	11.35
4	15/05/2025	2 h 38 min	6.22	8.68	11.60	11.50
5	16/05/2025	2 h 34 min	4.54	7.50	11.35	11.15
6	16/05/2025	4 h 3 min	3.20	6.23	12.35	11.60

Table A.3: Raw data from the preliminary propellant tests

Appendix B

Final tests data

This appendix contains the measurement data of the final tests.

B.1 PCB with 0.8 mm of orifice diameter

Tables B.1 and B.2 present all the raw data collected during the final tests using the PCB with a 0.8 mm orifice diameter. Table B.1 includes the test dates (the latest because some tests were repeated), the thermistor resistances, the external temperatures, as well as the current and voltage values on the tank. For the orifice heaters, the voltage and current were consistently maintained at 2.491 V and 0.061 A, respectively. In Table B.2, since the current and voltage values are the same, they are omitted; instead, the test duration and the initial and final mass of the propellant are reported.

Test n.	Date	Tank and orifice res. [kΩ]	Ext. temp. [°C]	Tank current [A]	Tank voltage [V]
1	19/07/2025	8.62; 6.04	25.7	0	0
2	19/07/2025	5.33; 4.77	25	0.491	2.037
3	07/07/2025	3.50; 3.80	23.5	0.692	2.887
4	19/07/2025	2.45; 3.17	26.2	0.842	3.564
5	07/07/2025	1.73; 2.65	23.5	0.963	4.154

Table B.1: Raw data from tank warming tests with the PCB having 0.8 mm of orifice diameter

Test n.	Date	Duration	Tank and orifice res. [kΩ]	Ext. temp. [°C]	In. and fin. mass [g]
1	12/07/2025	14 h 45 min	9.22; 6.49	24.0	10.9; 10.7
2	15/07/2025	14 h 57 min	5.71; 4.82	24.3	12.2; 10.5
3	14/07/2025	3 h 8 min	3.81; 3.75	24.3	13.05; 11.5
4	13/07/2025	7 h	2.70; 3.11	24.3	14.3; 7.9
5	14/07/2025	1 h 31 min	2.07; 2.64	24.0	11.5; 8.45

Table B.2: Raw data from propellant tests with the PCB having 0.8 mm of orifice diameter

B.2 PCB with 0.6 mm of orifice diameter

All raw data from the final tests conducted with the PCB featuring a 0.6 mm orifice diameter are reported in Tables B.3 and B.4. This section presents the same types of data as previously outlined, with the orifice voltage set to 2.000 V and current to 0.050 A.

Test n.	Date	Tank and orifice res. [kΩ]	Ext. temp. [°C]	Tank current [A]	Tank voltage [V]
1	18/07/2025	3.75; -	23.6	0.692	2.887
2	18/07/2025	2.45; -	23.6	0.842	3.564

Table B.3: Raw data from tank warming tests with the PCB having 0.6 mm of orifice diameter

Test n.	Date	Duration	Tank and orifice res. [kΩ]	Ext. temp. [°C]	In. and fin. mass [g]
1	17/07/2025	4 h 4 min	3.80; 3.46	23.8	12.50; 12.15
2	17/07/2025	3 h 7 min	2.53; 2.57	23.8	12.10; 11.80

Table B.4: Raw data from propellant tests with the PCB having 0.6 mm of orifice diameter